


University of Alberta

Design of Surface Acoustic Wave Micro-Electromechanical Sensors using
Finite Elements

by

Mohamed Mahmoud Taher EL Gowini 

A thesis submitted to the Faculty of Graduate Studies and Research
in partial fulfillment of the requirements for the degree of

Master of Science

Department of Mechanical Engineering

Edmonton, Alberta
Spring 2008



Library and
Archives Canada

Bibliothèque et
Archives Canada

Published Heritage
Branch

Direction du
Patrimoine de l'édition

395 Wellington Street
Ottawa ON K1A 0N4
Canada

395, rue Wellington
Ottawa ON K1A 0N4
Canada

Your file *Votre référence*
ISBN: 978-0-494-45805-1
Our file *Notre référence*
ISBN: 978-0-494-45805-1

NOTICE:

The author has granted a non-exclusive license allowing Library and Archives Canada to reproduce, publish, archive, preserve, conserve, communicate to the public by telecommunication or on the Internet, loan, distribute and sell theses worldwide, for commercial or non-commercial purposes, in microform, paper, electronic and/or any other formats.

The author retains copyright ownership and moral rights in this thesis. Neither the thesis nor substantial extracts from it may be printed or otherwise reproduced without the author's permission.

AVIS:

L'auteur a accordé une licence non exclusive permettant à la Bibliothèque et Archives Canada de reproduire, publier, archiver, sauvegarder, conserver, transmettre au public par télécommunication ou par l'Internet, prêter, distribuer et vendre des thèses partout dans le monde, à des fins commerciales ou autres, sur support microforme, papier, électronique et/ou autres formats.

L'auteur conserve la propriété du droit d'auteur et des droits moraux qui protègent cette thèse. Ni la thèse ni des extraits substantiels de celle-ci ne doivent être imprimés ou autrement reproduits sans son autorisation.

In compliance with the Canadian Privacy Act some supporting forms may have been removed from this thesis.

Conformément à la loi canadienne sur la protection de la vie privée, quelques formulaires secondaires ont été enlevés de cette thèse.

While these forms may be included in the document page count, their removal does not represent any loss of content from the thesis.

Bien que ces formulaires aient inclus dans la pagination, il n'y aura aucun contenu manquant.


Canada

Abstract

In a Surface Acoustic Wave (SAW) device the wave propagates along the surface, which makes it vulnerable to changes in the adjacent environment. In this study a 3D model of a SAW device was developed using Finite Elements. The model was applied to a case of hydrogen detection. The sensor was exposed to five concentration levels of hydrogen. The results of the model clearly illustrate the effect of hydrogen absorption on wave velocity. Subsequently, an idealization approach was adopted to change the full 3D model to a *Reduced* 3D model. The results of the reduced 3D model were compared with a 2D model, which is the configuration widely adopted in the literature. When comparing the results from both models with theoretical data, the reduced 3D model showed higher accuracy.

To my Parents

Acknowledgements

I would like to express my deepest thanks to my supervisor and mentor Dr Walied Moussa. It was his dedication and passion to the pursuit of knowledge that have inspired me throughout the course of my research work. Due to his continuous encouragement and support this thesis was completed with the highest standards.

I would also like to thank my parents and friends back home in Egypt and my dearest uncle Tarek. Their support and motivation have pushed me throughout the hardest times and made this work possible. It is because of our dearest ones that we continue to pursue the hardest paths.

Table of Contents

CHAPTER 1	1
1 INTRODUCTION	1
1.1 A Historical Perspective	1
1.2 Objective.....	3
1.3 Surface Acoustic Wave Devices.....	4
1.4 Thesis Structure.....	5
CHAPTER 2	7
2 LITERATURE REVIEW	7
2.1 Acoustic Wave Sensors	7
2.1.1 Shear Horizontal Acoustic Plate Mode Devices (SH-APM)	7
2.1.2 Flexural Plate Wave Devices (FPW)	8
2.1.3 Quartz Crystal Microbalance (QCM)	10
2.2 Modeling Techniques.....	10
2.2.1 Coupling of Modes (COM)	11
2.2.2 Equivalent Circuit Model	12
2.2.3 Finite Differences (FD).....	12
2.2.4 Finite Element Analysis (FEA)	13
CHAPTER 3	16
3 THEORY	16
3.1 Particle Displacement, Strain and Stress Fields	16

3.1.1	Particle Displacement Field.....	16
3.1.2	Strain Field.....	16
3.1.3	Stress Field.....	17
3.1.4	Elastic Constitutive Relations.....	18
3.1.5	Reduced Subscript Notation.....	18
3.2	Equation of Motion	19
3.3	Wave Equations.....	21
3.3.1	Wave Equation for Non-Piezoelectric Solids.....	21
3.3.2	Wave Equation for Piezoelectric Solids.....	22
3.4	Finite Element Formulation.....	25
3.5	Interdigital Transducers (IDT)	27
3.5.1	Delta Function Model.....	27
3.6	Surface Acoustic Wave Perturbation Mechanisms.....	29
3.6.1	Velocity and Attenuation Changes.....	30
CHAPTER 4	33
4	A 3D SURFACE ACOUSTIC WAVE SENSOR MODEL FOR HYDROGEN DETECTION	33
4.1	Introduction	33
4.2	Hydrogen Sensing Mechanisms.....	33
4.2.1	Pyroelectric Gas Analyzers (PGA).....	33
4.2.2	Fiber Optic Sensors (FOS).....	34
4.2.3	Electrochemical Sensors.....	34
4.2.4	Quartz Crystal Microbalance (QCM).....	35
4.3	The Hydrogen Palladium System.....	36

4.4	Finite Element Modeling of a SAW-IDT Sensor	37
4.4.1	Boundary Conditions.....	40
4.4.2	Transient Analysis.....	42
4.5	SAW Model for H₂ Absorption	45
4.5.1	YZ-LiNbO ₃ SAW Model	46
4.5.2	Modeling the Thin Palladium Film	50
4.5.3	Results.....	52
 CHAPTER 5		61
 5 A REDUCED 3D MODEL FOR SURFACE ACOUSTIC WAVE SENSORS.....		61
5.1	Introduction	61
5.2	Reduced 3D AlN/Si(111) Model	62
5.2.1	Boundary Conditions.....	65
5.2.2	Simulation Parameters	66
 CHAPTER 6		79
 6 CONCLUSIONS AND FUTURE WORK		79
6.1	Summary and Conclusions.....	79
6.2	Future Work	81
 References.....		79

Appendix.....	85
A. Finite Element Codes.....	85
A.1 Finite Element Code for XY-LiNbO₃ ZnO Model.....	85
A.2 Finite Element Code for YZ-LiNbO₃ ZnO Model for Hydrogen Detection.....	90
A.3 Finite Element Code for AlN/Si(111) Reduced 3D Model.....	95
A.4 Finite Element Code for AlN/Si(111) 2D Model	100

List of Tables

Table 1: Reduced Subscript Notation	19
Table 2: Parameters for XY-LiNbO ₃ ZnO Sensor	38
Table 3: Material Properties for Lithium Niobate	39
Table 4: Material Properties for Zinc Oxide.....	39
Table 5: Boundary Condition Table for XY-LiNbO ₃ ZnO Model	41
Table 6: Different Element Sizes for XY-LiNbO ₃ ZnO Model.....	43
Table 7: Comparison of Simulation Results with Published Results	44
Table 8: Boundary Condition Table for YZ-LiNbO ₃ Model.....	46
Table 9: Parameters for YZ-LiNbO ₃ SAW Sensor.....	47
Table 10: Parameters of YZ-LiNbO ₃ SAW Sensor with F _c 130MHz	50
Table 11: Thickness of the Palladium Film at Different Hydrogen Concentrations ...	51
Table 12: Material Properties of Pd Thin Film.....	52
Table 13: Simulation Results for Center Frequency and Insertion Loss for Different Hydrogen Concentration Cases using the Pd Coated YZ-LiNbO ₃ SAW Device Operating at F _c =130MHz.....	56
Table 14: Simulation for Phase Change Due to Various Hydrogen Concentrations in Pd Coated YZ-LiNbO ₃ SAW Device Operating at F _c =130MHz.....	57
Table 15: Material Properties of Aluminum Nitride.....	64
Table 16: Boundary Conditions for Reduced 3D AlN/Si(111) Model.....	65
Table 17: Parameters of the AlN/Si(111) Model Used in Mesh Sensitivity Analysis.	66

Table 18: Parameters for Mesh Sensitivity Analysis for AlN/Si(111) SAW Model...	67
Table 19: Theoretical Velocity Data for AlN/Si(111) Reduced 3D Model [53]	71
Table 20: Parameters of the AlN/Si(111) Models used in Comparison with Dispersion Curve Data	71
Table 21: Center Frequency Data for AlN/Si(111) Reduced 3D Model	74
Table 22: Comparison of Center Frequency Data of AlN/Si(111) Reduced 3D Model and 2D Model with Theoretical Frequency Data.....	75
Table 23: Comparison of Insertion Loss Data of AlN/Si(111) Reduced 3D Model and 2D Model	76

List of Figures

Figure 1: A SAW Device with Inter-Digital Electrodes.....	5
Figure 2: Symmetric and Anti-Symmetric Modes of Flexural Plate Waves	9
Figure 3: Delta Sources on Electrodes of IDT.....	28
Figure 4 Response of IDT-SAW Device in Delta Function Model.....	29
Figure 5: Schematic of XY-LiNbO ₃ ZnO Device Layout	37
Figure 6: Boundary Conditions Representation.....	41
Figure 7: FE Model of XY-LiNbO ₃ ZnO SAW Sensor.....	42
Figure 8: Mesh Sensitivity Analysis for XY-LiNbO ₃ ZnO Model.....	43
Figure 9: Verification of Simulation Results for XY-LiNbO ₃ ZnO Model.....	44
Figure 10: Layout of YZ-LiNbO ₃ SAW Device with Thin Pd Film	45
Figure 11: Mesh Sensitivity Analysis for YZ-LiNbO ₃ Model.....	47
Figure 12: Effect of Substrate Length on Center Frequency of YZ-LiNbO ₃ Model ...	49
Figure 13: Effect of Substrate Length on Insertion Loss of YZ-LiNbO ₃ Model.....	49
Figure 14: FE Model of YZ LiNbO ₃ Sensor Operating at $F_c = 130\text{MHz}$	50
Figure 15: Frequency Response of the YZ LiNbO ₃ Bare Device.....	52
Figure 16: A Close-up on the Frequency Response of the YZ LiNbO ₃ Bare Device Near $F_c=130\text{MHz}$	53
Figure 17: Frequency Response of SAW Sensor $F_c=130\text{MHz}$ with Pure Pd Film.....	53

Figure 18: Frequency Response of SAW Sensor $F_c=130\text{MHz}$ with 0.1 H/Pd Concentration.....	54
Figure 19: Frequency Response of SAW Sensor $F_c=130\text{MHz}$ with 0.2 H/Pd Concentration.....	54
Figure 20: Frequency Response of SAW Sensor $F_c=130\text{MHz}$ with 0.3 H/Pd Concentration.....	55
Figure 21: Frequency Response of SAW Sensor $F_c=130\text{MHz}$ with 0.4 H/Pd Concentration.....	55
Figure 22: Frequency Response of SAW Sensor $F_c=130\text{MHz}$ with 0.5 H/Pd Concentration.....	56
Figure 23: Phase Profiles at Different Hydrogen Concentrations Near the Center Frequency $F_c=130\text{MHz}$. The Inset Illustrates the Phase Profiles for the 0.3-0.5a.f. Concentration Region	57
Figure 24: Change in Phase Velocity Due to Hydrogen Absorption.....	58
Figure 25: The Change in First Lamé Constant with Respect to Change in Density of the Palladium Film at Different Hydrogen Concentrations	59
Figure 26: The Change in Second Lamé Constant with Respect to Change in Density of the Palladium Film at Different Hydrogen Concentrations.....	60
Figure 27: Insertion loss values at Different Hydrogen Concentrations.....	60
Figure 28: Schematic of AlN/Si(111) SAW Device.....	62
Figure 29: Silicon Crystal with Crystallographic Directions.....	63
Figure 30: Finite Element Model of AlN/Si(111) Reduced 3D Model	64
Figure 31: Electrodes in the Reduced 3D AlN/Si(111) Model.....	65

Figure 32: Mesh Sensitivity Analysis for 11um Thick AlN/Si(111) SAW Model.....	67
Figure 33: The Effect of Model Thickness on Center Frequency of the AlN/Si(111) Model.....	68
Figure 34: The Effect of Model Thickness on Insertion Loss of the AlN/Si(111) Model.....	68
Figure 35: The Effect of Substrate Length on Center Frequency of AlN/Si(111) Model.....	69
Figure 36: The Effect of Substrate Length on Insertion Loss of AlN/Si(111) Model.....	70
Figure 37: Time and Frequency Domain Responses for $h/\lambda=0.1$ AlN/Si(111) Configuration.....	72
Figure 38: Time and Frequency Domain Responses for $h/\lambda=0.11$ AlN/Si(111) Configuration.....	72
Figure 39: Time and Frequency Domain Responses for $h/\lambda=0.14$ AlN/Si(111) Configuration.....	73
Figure 40: Time and Frequency Domain Responses for $h/\lambda=0.17$ AlN/Si(111) Configuration.....	73
Figure 41: Time and Frequency Domain Responses for $h/\lambda=0.2$ AlN/Si(111) Configuration.....	74
Figure 42: Comparison between Simulation and Theoretical Frequency values for AlN/Si(111).....	75
Figure 43: Comparison of Center Frequency between Reduced 3D Model and 2D Model for AlN/Si(111).....	76
Figure 44: Comparison of IL Values for Reduced 3D Model and 2D Model for AlN/Si(111).....	77

Chapter 1

1 Introduction

1.1 A Historical Perspective

Surface Acoustic Waves (SAW) were first investigated by Lord Rayleigh [1]. The waves investigated were vertically polarized and propagating along the free surface of a homogenous isotropic elastic solid with their energies confined near the surface. Waves adopting these characteristics were later referred to as Rayleigh waves. In 1911 Love [2] illustrated that waves with shear horizontal polarization can propagate at the interface when a thin layer is added on top of the elastic solid under the condition that the wave velocity in the layer is slower than in the bulk material. More research was carried out by seismologists to have a better understanding of wave propagation and how it is related to earthquakes.

In 1965 White and Voltmer [3] reported the generation of SAW on a Quartz piezoelectric substrate. The waves were generated by applying a voltage signal to a set of finger-like electrodes spatially distributed on the device surface. A similar set of electrodes is placed further away from the input electrodes on the Quartz substrate to detect the propagating waves. This layout became known as the Delay Line structure. The SAW Delay Line offered an easy way of generating and detecting SAW on a piezoelectric substrate.

The advantages of the Delay line structure lead to its widespread use. The fabrication process of the SAW Delay line is based on the well established processes used for Integrated Circuits. This allows mass production of the devices at low cost. Another major advantage is the propagation of the waves on the surface. This property gives the user control over the wave therefore it can be easily sampled, modified according to the desired application. Since acoustic wave velocities are

almost five orders of magnitude slower than electromagnetic waves small size devices can be fabricated.

Research directed towards understanding the properties of SAW delay lines and their possibilities have lead to various applications. Initially, SAW delay lines were mostly used in electronic devices such as radars to optimize the signal to noise ratio and in pulse compression, as band-pass filters in TV and as resonators. However, the confinement of a SAW near the surface of the substrate has allowed it to be sensitive to changes in the adjacent environment. This property lead to the use of SAW devices in many sensing applications such as in detection of gas, viscosity, temperature, humidity, strain, force etc. In addition, a wide range of acoustic devices other than the SAW device were developed such as the Quartz Crystal Microbalance (QCM), Shear Horizontal Acoustic Plate Mode Devices (SH-APM), Flexural Plate Wave Devices (FPW).

When designing a sensor for a given application there are many parameters that need to be selected and often there are many choices available. Among the parameters that need to be chosen is the piezoelectric substrate, the operating frequency of the device, the materials of the electrodes, shape of electrodes, etc. In order to save both time and money modeling often is the best option available. Building models gives the designer the ability to test different parameters and also to test the hypothesis or the response of the sensor under certain conditions. Modeling therefore plays an important role in the design phase.

1.2 Objective

The purpose of this study is to develop a Finite Element model of a Surface Acoustic Wave Device. The model is expected to be a tool in the designer's hand when designing Surface Acoustic Wave Devices primarily for sensing applications.

Configurations of SAW devices vary according to the materials used. SAW devices could consist of a bare substrate with electrodes on the free surface, a layered device with electrodes at the interface or at the surface. In this study different configurations will be adopted at different stages and the results corresponding to each model will be verified either with experimental or theoretical data.

Finally, the model should be optimized such that it does not require a prolonged run time. The simulation run time is one of the important issues associated with Finite Element analysis. This feature would give the designer freedom in testing as many cases as possible and essentially developing an optimum SAW sensor for a given application.

1.3 Surface Acoustic Wave Devices

A SAW device consists of a piezoelectric material, which is the medium in which the wave propagates. In some configurations as will be seen later in this study, a SAW device consists of a thin piezoelectric layer on top of a non-piezoelectric substrate such as Silicon. In this case the SAW propagates in both materials. The piezoelectric film allows electrical excitation of the SAW in a non-piezoelectric material. The signal is usually applied to the piezoelectric material by means of electrodes. Usually these electrodes have an Inter-digital geometry as illustrated in Figure 1. There are two sets of electrodes on the surface of the piezoelectric substrate. One is for actuating the SAW and the other is for receiving the signal.

The distance between both sets of electrodes is the propagation area. This region is where the wave interacts with the measurand to produce a noticeable change at the receiving end. Often when the sensor is used for chemical detection a thin film is deposited in this region. The film is usually chosen to be chemically selective to the gas or chemical under test. As the film interacts with the chemical its properties will change accordingly. When the wave propagates at the surface and encounters the film, the film properties will influence the propagation properties of the waves. The received signal at the output electrodes indicates the changes in wave properties.

As the wave propagates along the surface of the device, Y-axis in Figure 1 the particles can oscillate along any or all of the three axis. When the particles oscillate along the Y-axis this is called a Longitudinal wave. When the particles oscillate along the Z-axis this is called a Shear Vertical wave. When the oscillations are along the X-axis this is called a Shear Horizontal wave.

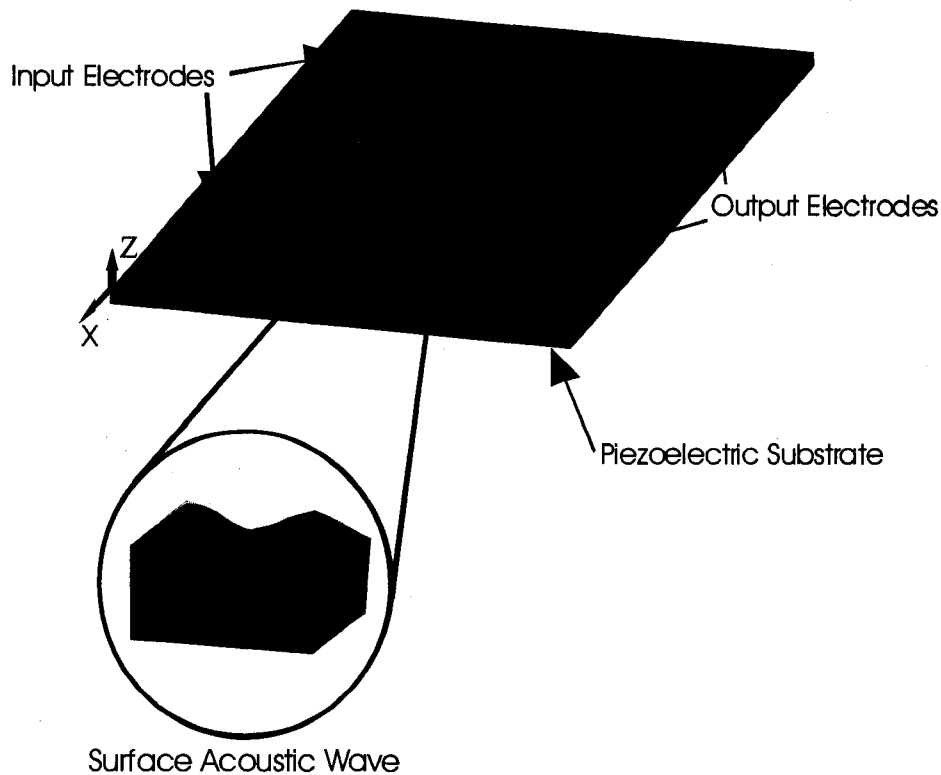


Figure 1: A SAW Device with Inter-Digital Electrodes

1.4 Thesis Structure

This thesis is structured as follows. Chapter 2 provides a literature review on the different acoustic wave devices and gives examples of their sensing applications. In addition, it describes the different modeling techniques of surface acoustic wave devices. It focuses on examples of finite element analysis of SAW devices.

Chapter 3 provides the theory of wave propagation. It introduces the Stress, Strain and Particle Displacement fields. Then it continues to derive the equation of motion of a vibrating particle. Then the derivation of the wave equation in a non-piezoelectric solid is presented. The piezoelectric constitutive equations are then introduced and the wave equations are derived in a similar way to the non-piezoelectric solid. Subsequently, the theory of SAW devices excited by interdigital Electrodes is presented. Finally, changes in wave properties such as wave velocity and attenuation

as a result of interaction with the measurand are related to the energy and power densities of the waves.

Chapter 4 introduces the first model that was built and its verification with simulation and experimental results from the literature. The model is then applied to a case of hydrogen detection. A Palladium film is placed along the propagation area as a chemically selective film for hydrogen. Different hydrogen concentrations are applied and the sensor response to the different cases is shown. The change in wave velocity in each case is plotted. The magnitude of the velocity change is related to the change in properties of the Palladium film. Finally, the insertion loss that takes place due to different concentration values is shown.

Chapter 5 introduces an optimization approach that was applied to the model. The model size was significantly reduced through implementing a reduced 3D model. The performance of the reduced 3D model was compared with theoretical data from the literature. The results showed very good agreement and the run time of the model was significantly reduced. A 2D model was built and its accuracy was compared with that of the reduced 3D model, because 2D models are widely implemented in the literature. On comparing with theoretical data the reduced 3D model yielded more accurate results.

Chapter 6 summarizes the methodologies and findings in this study and lists the future work that should take place from the point this study was concluded.

Chapter 2

2 Literature Review

2.1 Acoustic Wave Sensors

The characteristic feature of acoustic devices that the propagating waves can be *perturbed* by surface interactions has led to their widespread use in sensing applications. The most commonly used methodology for acoustic sensing is through depositing a thin film along the propagation path. The film properties change due to changes in the external environment. The changes in film properties induces corresponding changes in wave characteristics such as velocity changes and attenuation. Acoustic sensors are very well established in the literature as chemical sensors.

The most commonly used acoustic sensors are presented here. Their operating principle is briefly introduced with some applications. The acoustic wave devices are the Quartz crystal microbalance, Shear Horizontal Acoustic Plate Mode (SH APM) device, Flexural Plate Wave device (FPW) and Surface Acoustic Wave (SAW) devices. The SAW device is the focus of this research, therefore it is presented in details in the following chapters.

2.1.1 Shear Horizontal Acoustic Plate Mode Devices (SH-APM)

This class of acoustic sensors involves acoustic waves propagating along the surface with particle polarization in the Shear Horizontal direction. There is no polarization in the surface normal direction. This feature allowed SH-APM devices to be widely used in liquid sensing applications since the wave can propagate while in contact with liquids without significant attenuation. The Rayleigh wave on the other hand has surface normal polarization and therefore dissipates most of its energy when

in contact with liquid since the surface normal displacement components generate compression waves in the liquid [4].

SH-APM devices utilize thin piezoelectric substrates usually a few wavelengths thick. Commonly used substrates are Quartz, Lithium Niobate and Lithium Tantalate [5]. The wave propagates along the surface between the input and output transducers. The wave energy is distributed throughout the thickness, therefore sensitivity depends on the thickness and both surfaces can be used for sensing applications. This features is very useful if the sensor is placed in an environment that could ruin the IDT electrodes. In such applications the bottom surface is used as the sensing surface, while the IDT's are isolated. The SH-APM device detects changes in the adjacent liquid such as conductivity, viscosity, mass loading, permittivity, etc.

Kondoh *et al* [5] fabricated a 36° YX-Lithium Tantalate (LiTaO_3) acoustic device, which propagates the SH mode. The device was used for detecting an enzyme reaction in solution. The reaction lead to changes in the pH value of the liquid, which changed the electrical properties of the wave and hence changed the wave velocity. Martin *et al* [6] used a 36° YX-Lithium Tantalate (LiTaO_3) SH-APM device to detect density and viscosity changes in the adjacent solution. Changes in density and viscosity of the adjacent solution were detected as changes in wave velocity and attenuation. Josse *et al* [7] used a 36° YX-Lithium Tantalate (LiTaO_3) SH-APM device to detect various concentrations of analytes in solutions. The increasing concentrations of analytes lead to increasing frequency shift and insertion loss. Since the SAW device was coated with a chemically selective film, increasing analyte concentration lead to further absorption by the film. Changes in the viscoelastic properties of the film due to absorption perturbed the wave propagation.

2.1.2 Flexural Plate Wave Devices (FPW)

This class of acoustic sensors utilizes the propagation of waves in very thin substrates, just a few microns thick [4]. By adjusting the device thickness the FPW velocity can be reduced to be much lower than that of SAW [4]. This is a highly desirable property especially for liquid sensing because the wave would not radiate

any of its energy into the liquid. Another quality is the high sensitivity of the substrate to mass loading. The fine thickness of the substrate increases its sensitivity appreciably to mass loading, therefore making the device an ideal candidate for bio-sensing applications. There are two modes of wave propagation in FPW devices Figure 2. The Symmetric mode where the particle displacements are symmetric about the neutral plane of the plate and the Anit-symmetric mode, where the displacements have odd symmetry about the neutral plane of the plate [4]. The sensing mechanism of FPW devices involves changes in the wave velocity and attenuation due to interaction with the surrounding environment.

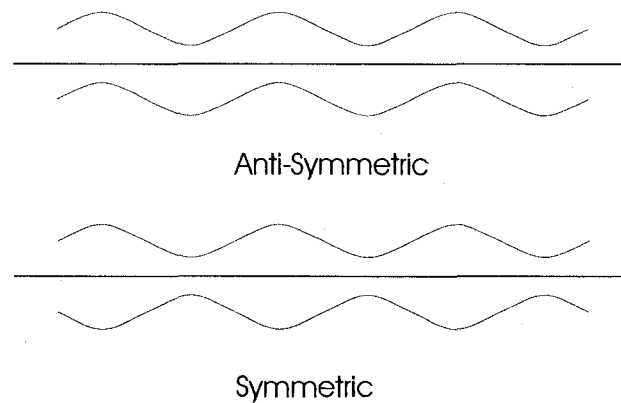


Figure 2: Symmetric and Anti-Symmetric Modes of Flexural Plate Waves

Lee *et al* [8] fabricated a FPW device using a thin Lead-Zirconium-Titanate (PZT) film on a Silicon substrate. The device was used for detection of bio-materials (Biotin Streptavidin). For this application the surface of the device was coated with a chemically selective film to facilitate the absorption process. The operating frequency of the device was 3MHz and the sensor resolution was 2.07ng cm^2 . The sensor response to changes in mass loading was illustrated by corresponding shifts in center frequency.

Black *et al* [9] performed a comparative analysis on the sensitivities of a FPW device with respect to a SAW device. The comparisons were performed using several coating layers on both devices. In addition, the devices were exposed to different vapors. The frequency shifts of both devices were found to be linearly proportional to the gas concentrations. The FPW device was found to be more sensitive than the

SAW device in all cases. The higher sensitivity of the FPW is due to the device response to mass loading and gas density.

2.1.3 Quartz Crystal Microbalance (QCM)

The QCM is also referred to as the Thickness Shear Mode (TSM) resonator. The QCM consists of a thin disk Quartz crystal with two electrodes patterned on both sides. A voltage signal applied across the electrodes induces shear wave propagation in the thickness of the quartz crystal. The wave oscillates back and forth and the oscillation frequency is proportional to the mass of the crystal.

The surface of the QCM is the sensing medium. The QCM can be used for mass loading, viscosity and density changes. When the QCM is used as a chemical sensor a thin film is deposited on the surface and absorption of gas molecules leads to mass changes on the surface which are detected as frequency shifts [4].

Schofield *et al* [10] used an AT-cut 5MHz Quartz crystal for continuous monitoring of cell attachment and formation of a thin bio-film layer on the QCM surface. A buffer medium containing the cells was allowed to flow over the QCM and the sensor response was recorded over time to determine the frequency shifts and dissipation due to cell adhesion. The mass of the cells on the surface of the device were correlated to the corresponding frequency shift.

There are various applications in the literature for the use of QCM in gas detection. Examples in the literature for the use of QCM in hydrogen gas detection are given in a later chapter dedicated to the study hydrogen detection.

2.2 Modeling Techniques

Designing SAW devices by trial and error experiments is both time consuming and expensive. The rapid development of the computer industry has allowed the incorporation of computer simulations in the design process. Computer simulations give designers the ability to test various designs and change as many parameters as possible, therefore designers can have a deeper understanding of the physical

phenomena involved while maintaining costs at a low level. Various modeling techniques of SAW devices are available, this is due to the significant amount of effort put forward by researchers to develop models that accurately resemble the actual device.

2.2.1 Coupling of Modes (COM)

The device parameters are represented as a set of transfer matrices. Generally there are three parameters for the SAW device (IDT's, Center-to-Center distance and Reflectors) hence three Transfer Matrices for the COM technique. The output signal is calculated from the product of the Transfer matrices with the matrix representing the input signal. Wang *et al* [11] and Suzuki *et al* [12] used the COM method to analyze SAW device parameters. In both cases the output of the COM analysis was used either as a reference or input for further analysis techniques on device performance. The COM method is more commonly used when designing SAW filters because it can more accurately determine the influence of parameters such as electrode thicknesses, electrode overlap and can take into consideration factors such as SAW interaction at the electrode, forward and backward reflections, etc. Ntagwirumugara *et al* [13] used the COM analysis to optimize the design of a AlN/ZnO/Si SAW device in terms of device geometry, electrode location, and electrode geometry. Several parameters were changed in the simulations such as electrode number and thickness as well as the operating frequency. When modeling SAW devices for sensor applications other modeling techniques such as Finite Element method can be used to complement the COM technique in determining the SAW response to a measurand. Lee *et al* [14] developed a SAW sensor for compression force measurement. The COM method was used to determine the optimum set of device parameters and the Finite Element Analysis was used to analyze the deformation due to applied pressure.

2.2.2 Equivalent Circuit Model

An equivalent circuit to the SAW device has been developed to model device performance. In the equivalent circuit model each IDT is represented as a three port network, two are the electrical equivalents of the acoustic ports and the third is an actual electrical port. Through the third port the signals are applied and received. The electrical elements in the circuit are calculated from wave and device properties such as wave velocity, substrate electromechanical coupling coefficient, center frequency, number of electrode pairs etc. The current and voltage in each port are related through the elements of the admittance matrix. The two networks corresponding to the IDT's are combined together in a two port network. The overall transfer function of the SAW device is determined from the ratio of the output to input voltage, which are calculated using the elements of the modified admittance matrix. A thorough illustration of the equivalent circuit model is available in Campbell [15]. The equivalent circuit can accurately determine the frequency response of SAW devices and the model can incorporate parameters such as device impedance levels and the influence of second order effects on frequency response [15]. Liu and Cui [16] used the equivalent circuit model to determine the effect of parameters such as operating frequency, center-to-center distance and piezoelectric substrate thickness for layered devices on power consumption. In addition, Inagawa [17] used the equivalent circuit model to determine the effect of electrode thickness and spacing on device response for different electrode arrangements.

2.2.3 Finite Differences (FD)

Wong and Tam [18] utilized the Finite Difference Time Domain (FDTD) technique to model the frequency response of a SAW device. The model was 2-D and assumed that the displacement field and the electric potential do not vary in the shear horizontal direction. In addition, the electrodes were modeled with zero thickness to eliminate the second order effects due to the electrode mass from the analysis. Two models were developed. The first model involved a Zinc Oxide substrate with IDT electrodes. This model was used to test for the influence of the number of electrodes on the frequency response. The second model involved a ZnO/Diamond/Si-layered

SAW filter. The frequency response of the layered device was compared with experimental results and there was a highly noticeable discrepancy. Jatkar and Beker [19] used the Finite Difference method to model the influence of package pin dimensions and wire bond length on the frequency response of a SAW device. The FD method was used to calculate the charge density on the IDT's and determine its frequency response. The conduction currents generated due to package pins and bond wires were determined using a current simulation technique and their values were input in the FD model. The model was 3-D and involved a YZ-LiNbO₃ substrate. Results indicated that distortion to the response is not significant and hence can be neglected.

2.2.4 Finite Element Analysis (FEA)

Finite Element Analysis (FEA) has been widely used in the literature to model SAW devices. Various examples in this section are provided to highlight the use of FE modeling of SAW devices. Lerch [20] used FEA to determine the vibration modes of piezoelectric transducers with different shapes in 2-D and 3-D. The results were compared with experimental studies and were in good agreement.

Ippolito *et al* [21], developed a 3-D FE model of a X-cut Y-propagating Lithium Niobate substrate (XY-LiNbO₃) with IDT electrodes. The device surface was completely covered with a 3µm thick Zinc Oxide (ZnO) layer. They used the model to determine the frequency response of the device and compared their simulation results with their experimental work. The device was excited with an Impulse signal and the frequency response was obtained from the time domain signal using Fourier Transform. The results were agreeable. In addition, the model was used to determine the change in response due to shorting the device surface as in the case of gas absorption. Ippolito *et al*, [22] also developed a 2-D model with the same device configuration in the 3-D, however the third dimension was eliminated in the analysis. The frequency response from the 2-D simulation showed high discrepancy when compared with experimental results because the 2-D model neglects displacements in the shear transverse direction.

Atashbar *et al*, developed a 3-D FE model [23] for a XY-LiNbO₃ SAW-IDT sensor for Hydrogen detection. A thin Palladium film was used as the chemically selective layer. The model was excited with an impulse signal. Their study involved only one case of hydrogen absorption. The change in insertion loss and time delay of the wave were observed. The model developed by Atashbar *et al* suffers from some defects. Wave reflection at the boundaries was causing interference with the sensor response. This was because the effect of the boundaries in the direction of wave propagation was not eliminated by extending the boundaries or by adopting damping coefficients. In addition, interference from the bottom surface also influenced the sensor response since it was not at a far enough depth.

Liu and Cui [16] recently published a 3-D FE model of a SAW sensor on a piezoelectric Zinc Oxide (ZnO) substrate. Their analysis was quite different. Their objective was to determine the influence of changing the device parameters on power consumption. Output from the FE model was used in developing an equivalent circuit model using PSPICE in order to determine the overall power consumption.

Botkin *et al* [24] developed a FE model for bio-sensing. The model was 3-D and it was assumed that all the fields vary in the longitudinal and shear vertical directions only and hence the wave was uniform in the shear horizontal direction. As all the variations took place in two dimensions, the model was referred to by the authors as a 2-D model. The model consisted of a thin Silicon Dioxide (SiO₂) film on a piezoelectric CT-cut Quartz crystal with Gold electrodes at the interface. A fluid layer was modeled on top of the SiO₂ layer. Wave propagation properties in the substrate and the thin film due to adding solutes to the fluid were studied.

Xu [25] developed a FE model of a SAW device on a YZ-LiNbO₃ substrate. The model developed was 2-D, therefore the displacements in the shear horizontal direction were eliminated from the calculations. In the analysis damping coefficients along the boundary were imposed to reduce reflection and interference with the signal. The SAW device was excited by an impulse signal. The model was used to

determine the effect of increasing the number of electrodes on sensor response. Insertion loss decreased due to increasing the number of electrode pairs as expected.

Xu and Jiang [26] used the model in the previous study to determine the effect of electrode mass on sensor response. Instead of modeling the electrodes as a set of nodes coupled by a volt degree of freedom as in the previous case, they were modeled as solid electrodes. The results indicated that the influence of electrode mass is noticeable at frequencies in the Gigahertz range and can not be ignored, however when the operating frequency is in the range of a few Megahertz the electrode mass has negligible effect on sensor response.

Chapter 3

3 Theory

3.1 Particle Displacement, Strain and Stress Fields

Surface Acoustic Waves are mechanical vibrations that take place in a medium. Characterizing the wave and deriving the wave equation requires several parameters to be determined, these are the particle displacement field, strain field and the stress field.

3.1.1 Particle Displacement Field

The particle displacement field $\mathbf{U}(\mathbf{r},t)$ describes the displacements of all the particles in the medium at any point in time. The displacement field for a wave propagating along the x-direction is [4]

$$U(\mathbf{r},t) = (U_1x + U_2y + U_3z) e^{j(\omega t - kx)} \quad (3-1)$$

where the U_i 's are the particle displacement components in the x , y and z directions, k is the wave number ($k = 2\pi/\lambda$), ω is the angular frequency ($\omega = 2\pi f$) in rad/s.

3.1.2 Strain Field

Deformation in a material occurs when neighboring particles are displaced relative to each other. In order to measure the deformation in a material a quantity defined as difference between the relative positions of two points is used. From this quantity the linearized Strain field $S_{ij}(\mathbf{r},t)$ can be derived. The derivation is presented thoroughly in [27].

$$S_{ij} = \frac{1}{2} \left(\frac{du_i}{dr_j} + \frac{du_j}{dr_i} \right) \quad ; i, j = x, y, z \quad (3-2)$$

The strain components can be grouped into a matrix that has the following representation;

$$[S] = \begin{pmatrix} S_{xx} & S_{xy} & S_{xz} \\ S_{yx} & S_{yy} & S_{yz} \\ S_{zx} & S_{zy} & S_{zz} \end{pmatrix}$$

From the definition of the Strain field given in (3-2) it can be seen that the strain matrix is symmetric hence $S_{ij} = S_{ji}$.

3.1.3 Stress Field

Propagation of Surface Acoustic waves in a body can be initiated by applying forces at the surface, which are transmitted to the interior through elastic forces between neighboring particles. Stresses are therefore induced on interfacial surfaces between neighboring particles. These stresses are also termed Internal Traction Forces $T_{ij}(\mathbf{r}, t)$ and have the units N/m^2 . The traction forces acting on the planes of a volume element have three components in a Cartesian coordinate system. Grouping the traction forces in the x , y and z planes give [27];

$$\begin{aligned} T_x &= (T_{xx})x + (T_{yx})y + (T_{zx})z \\ T_y &= (T_{xy})x + (T_{yy})y + (T_{zy})z \\ T_z &= (T_{xz})x + (T_{yz})y + (T_{zz})z \end{aligned} \quad (3-3)$$

T_{ij} is the traction force on the j^{th} plane in the i^{th} direction. For the general case where a volume element has an arbitrary oriented plane \mathbf{n} , the components T_{in} can be expressed in terms of the traction forces acting on the x , y and z planes as illustrated below [27];

$$\begin{bmatrix} T_{xn} \\ T_{yn} \\ T_{zn} \end{bmatrix} = \underbrace{\begin{bmatrix} T_{xx} & T_{xy} & T_{xz} \\ T_{yx} & T_{yy} & T_{yz} \\ T_{zx} & T_{zy} & T_{zz} \end{bmatrix}}_{\text{Stress Matrix}} \begin{bmatrix} n_x \\ n_y \\ n_z \end{bmatrix}$$

the n_i elements are the x , y and z components of the unit vector \hat{n} normal to the n^{th} plane. The symmetry of the stress matrix will be highlighted in the derivation of the equation of motion.

3.1.4 Elastic Constitutive Relations

The stresses induced between neighboring particles during wave propagation are linearly proportional to the strain as long as deformation is within the elastic region of the material (Hooke's Law). If the stresses increase further, irreversible plastic deformation can take place in the material. The plastic region is normally not of interest in the study of acoustics [27].

The applied stress is related to the strain through the elastic constants of the material;

$$T_{ij} = c_{ijkl} S_{kl} \quad ; i, j, k, l = x, y, z \quad (3-4)$$

which shows that there are 81 elastic stiffness constants. Not all of the 81 elastic constants are unique. The symmetry of the stress and strain matrices induces symmetry between the elastic constants. The maximum number of elastic constants for a medium with general crystal symmetry is 21. The number of independent elastic constants in the stiffness matrix decreases as crystal symmetry increases and reduces to two for isotropic materials c_{12} and c_{44} .

3.1.5 Reduced Subscript Notation

Symmetry of both the stress and strain matrices result in six unique elements out of all the nine elements in the matrix. For this reason a reduced notation has been

introduced where the two lower case subscripts ij are replaced by one upper case subscript. Table 1 illustrates the transformation of subscripts

The reduced notation can be extended to the elastic constants as long as the stress matrix is symmetric, hence c_{ijkl} is rewritten as c_{IJ} . The stress-strain relation in reduced notation has the following form;

$$T_I = c_{IJ} S_J \quad (3-5)$$

This notation facilitates the handling of equations where variables/constants may have too many subscripts.

Table 1: Reduced Subscript Notation

<i>Double Subscripts</i>	<i>Reduced Notation</i>	<i>Matrix Representation</i>
xx	1	$\begin{pmatrix} T_1 & T_6 & T_5 \\ T_6 & T_2 & T_4 \\ T_5 & T_4 & T_3 \end{pmatrix}$
yy	2	
zz	3	
yz or zy	4	
xz or zx	5	
xy or yx	6	

3.2 Equation of Motion

The forces acting on a vibrating volume element with volume δV and surface area δA are body forces $F \delta V$ and surface traction forces $\int_{\delta S} T \cdot \hat{n} dS$

Newton's law states [27];

$$\int_{\delta S} T \cdot \hat{n} dS + \int_{\delta V} F dV = \int_{\delta V} \rho \frac{\partial^2 \bar{u}}{\partial t^2} dV \quad (3-6)$$

where ρ refers to particle density. In this study body forces such as gravity are assumed to have a negligible effect therefore, the F term will be eliminated from the derivation of the equation of motion. Since the particle volume is very small, therefore the integrands are assumed to be constant [27]

$$\frac{\int_{\delta S} \mathbf{T} \cdot \hat{\mathbf{n}} dS}{\delta V} = \rho \frac{\partial^2 \bar{\mathbf{u}}}{\partial t^2} \quad (3-7)$$

using the following substitution [27]

$$\nabla \cdot \mathbf{T} = \lim_{\delta V \rightarrow 0} \frac{\int_{\delta S} \mathbf{T} \cdot \hat{\mathbf{n}} dS}{\delta V} \quad (3-8)$$

the translational equation of motion for a volume element becomes [27]

$$\nabla \cdot \mathbf{T} = \rho \frac{\partial^2 \bar{\mathbf{u}}}{\partial t^2} \quad (3-9)$$

where $\nabla \cdot \mathbf{T}$ is the Divergence of \mathbf{T} and is expressed as [27]

$$\nabla \cdot \mathbf{T} = \left(\frac{\partial}{\partial x} T_x + \frac{\partial}{\partial y} T_y + \frac{\partial}{\partial z} T_z \right) \quad (3-10)$$

which can be expanded as follows

$$\begin{aligned} \nabla \cdot \mathbf{T} = & \left(\frac{\partial}{\partial x} T_{xx} + \frac{\partial}{\partial y} T_{xy} + \frac{\partial}{\partial z} T_{xz} \right) \bar{x} \\ & + \left(\frac{\partial}{\partial x} T_{yx} + \frac{\partial}{\partial y} T_{yy} + \frac{\partial}{\partial z} T_{yz} \right) \bar{y} \\ & + \left(\frac{\partial}{\partial x} T_{zx} + \frac{\partial}{\partial y} T_{zy} + \frac{\partial}{\partial z} T_{zz} \right) \bar{z} \end{aligned} \quad (3-11)$$

the expansion of $\nabla \cdot \mathbf{T}$ leads to a much simpler form of the equations of motion

$$\sum_{j=1}^3 \frac{\partial}{\partial r_j} T_{ij} = \rho \frac{\partial^2 u_i}{\partial t^2} \quad (3-12)$$

The effects of particle rotations and body torques have been ignored since they have negligible effects [27], therefore the stress matrix is always symmetric

$$T_{ij} = T_{ji} \quad (3-13)$$

3.3 Wave Equations

The wave equations for non-piezoelectric solids and piezoelectric solids are going to be derived. The same procedure is applied for both cases, however for the piezoelectric case the mechanical displacements and the voltage are coupled through the piezoelectric constitutive equations.

3.3.1 Wave Equation for Non-Piezoelectric Solids

Having derived the equation of motion for a volume element in a vibrating medium, the wave equation can be derived by combining the equation of motion and the elastic constitutive relations of the medium. Using the symmetry of the strain matrix, the component T_{ij} , which is expressed as;

$$T_{ij} = \sum_{k,l=1}^3 c_{ijkl} S_{kl} \quad (3-14)$$

can be rewritten as

$$T_{ij} = \sum_{k,l=1}^3 c_{ijkl} \frac{\partial u_k}{\partial r_l} \quad (3-15)$$

substituting this expression into the equation of motion (3-12) results in the wave equation for the non-piezoelectric medium.

$$\sum_{j,k,l=1}^3 c_{ijkl} \frac{\partial^2 u_k}{\partial r_j \partial r_l} = \rho \frac{\partial^2 u_i}{\partial t^2} \quad ; i = x, y, z \quad (3-16)$$

For illustrative purposes assume a surface acoustic wave is propagating along the x -direction of a cubic crystal. Due to cubic symmetry there are three independent elastic constants c_{11} , c_{12} and c_{44} . The wave equations are

$$\begin{aligned} \rho \frac{\partial^2 u_x}{\partial t^2} &= c_{11} \frac{\partial^2 u_x}{\partial x^2} \\ \rho \frac{\partial^2 u_y}{\partial t^2} &= c_{44} \frac{\partial^2 u_y}{\partial x^2} \\ \rho \frac{\partial^2 u_z}{\partial t^2} &= c_{44} \frac{\partial^2 u_z}{\partial x^2} \end{aligned} \quad (3-17)$$

The first equation is a Longitudinal wave with polarization along the direction of propagation. The second equation is a Shear Vertical wave with polarization in the y-direction. The third equation is a Shear Horizontal wave with the polarization in the z-direction.

3.3.2 Wave Equation for Piezoelectric Solids

It was illustrated above for non-piezoelectric solids that the wave equations are generated by substituting the elastic constitutive relation in the equation of motion. The constitutive relations for piezoelectricity are quite different than for non-piezoelectric solids. In the following the constitutive relations of piezoelectricity are presented and the derivation of the wave equations are derived.

3.3.2.1 Piezoelectric Constitutive Equations

Some materials are electrically polarized when they are mechanically strained. When the material is mechanically deformed the atoms are displaced as well as the electrons within the atoms leading to the occurrence of microscopic dipole moments. These dipole moments add up constructively to generate a macroscopic dipole moment in the material and hence the presence of electric charges on the surface of the material. This is called the Direct Piezoelectric effect. A material that responds in this manner to mechanical strain adopts the Converse piezoelectric effect as well, where an applied electric field generates mechanical strain in the material. Piezoelectricity is a versatile property that is highly desirable in sensing applications and provides an effective means of generating and receiving surface acoustic waves.

To account for the piezoelectric effect Hooke's law should be modified to include the electrical interaction that takes place in the material. The piezoelectric constitutive relations have various forms in the literature, the equations presented here are termed the Piezoelectric Stress equations where the Strain is an independent variable. Summation over repeated subscripts is assumed [28].

$$\begin{aligned}
T_{ij} &= c_{ijkl}^E S_{kl} - e_{ijk}^T E_k \\
D_i &= \varepsilon_{ij}^S E_j + e_{ikl} S_{kl}
\end{aligned}
\tag{3-18}$$

where \mathbf{D} is the electric displacement field and has units of C/m^2 (Coulomb per square meter), ε_{ij} is the dielectric permittivity constants and have units F/m (Farad per meter), E_j is the electric field components and have units of V/m (Volt per meter) and the constants e_{ijk} and e_{ikl} are the piezoelectric stress constants and have units C/m^2 . The piezoelectric stress matrices in both equations are transposes of one another, hence the superscript T . The piezoelectric matrix couples the electric and mechanical fields. The superscripts on the elastic stiffness constants and the dielectric permittivity constants imply that these are the properties at constant electric field and strain respectively.

3.3.2.2 Deriving the Wave Equations

Waves propagating in a piezoelectric crystal involve coupling of the particle displacement and the electric and magnetic fields. The equation of motion is coupled with Maxwell's equations for electromagnetic fields through the piezoelectric constitutive equations, however this coupling is weak [29].

Since the solutions of interest are the acoustic waves, the magnetic field is assumed to be static and the electric field is calculated as the gradient of the potential. This approximation is termed the Quasi-Static approximation and has negligible effects on the solution [28]. Due to the quasi-static approximation the electric field components are expressed as;

$$E_i = -\frac{\partial \phi}{\partial r_i}
\tag{3-19}$$

At this stage the wave equation can be easily derived from the piezoelectric constitutive relations and the equation of motion. Substituting the stress (3-15) in the equation of motion ((3-12) and replacing the electric field with the negative gradient of the scalar potential yields

$$c_{ijkl}^E \frac{\partial^2 u_k}{\partial r_j \partial r_i} + e_{ijk} \frac{\partial^2 \phi}{\partial r_k \partial r_j} = \rho \frac{\partial^2 u_i}{\partial t^2} \quad (3-20)$$

this is the first second order coupled wave equation.

Divergence of the second piezoelectric constitutive equation yields

$$\frac{\partial D_i}{\partial r_i} = \frac{\partial}{\partial r_i} \left(\varepsilon_{ij}^S \frac{\partial \phi}{\partial r_j} \right) + e_{ikl} \frac{\partial^2 u_k}{\partial r_l \partial r_i} \quad (3-21)$$

since piezoelectric materials are insulating materials $\frac{\partial D_i}{\partial r_i} = 0$ due to the absence of

electric charge within the material. The second wave equation therefore is

$$\varepsilon_{ik}^S \frac{\partial^2 \phi}{\partial r_i \partial r_k} = e_{ikl} \frac{\partial^2 u_k}{\partial r_l \partial r_i} \quad (3-22)$$

equations (3-20) and (3-22) are two second order coupled wave equations in $i,j,k,l = x,y,z$ and summation over repeated subscripts is assumed. Solution of these equations yields four partial wave equations; displacement equations with polarizations in 3 directions and the voltage equation.

For illustrative purposes consider the shear wave propagating along the x -direction of an Aluminum Nitride (AlN) crystal with polarization along the z -axis. After substitution of the appropriate material property matrices and algebraic manipulation, the wave equations for the z -polarized x -propagating shear wave can be written in the abbreviated subscript notation as

$$\begin{aligned} \rho \frac{\partial^2 u_z}{\partial t^2} &= c_{55} \frac{\partial^2 u_z}{\partial x^2} + e_{x5} \frac{\partial^2 \phi}{\partial x^2} \\ \varepsilon_{xx} \frac{\partial^2 \phi}{\partial x^2} &= e_{x5} \frac{\partial^2 u_z}{\partial x^2} \end{aligned} \quad (3-23)$$

The second equation is used to eliminate the potential from the first equation yielding

$$\left(c_{55} + \frac{e_{x5}^2}{\varepsilon_{xx}} \right) \frac{\partial^2 u_z}{\partial x^2} = \rho \frac{\partial^2 u_z}{\partial t^2} \quad (3-24)$$

substituting

$$c'_{55} = \left(c_{55} + \frac{e_{x5}^2}{\epsilon_{xx}} \right) \quad (3-25)$$

equation (3-24) resembles the wave equation for non-piezoelectric solids (3-16). The stiffness constant c'_{55} can be expressed as

$$c'_{55} = c_{55} \left(1 + \frac{e_{x5}^2}{c_{55}\epsilon_{xx}} \right) \quad (3-26)$$

The increase in value of the elastic constants is known as Piezoelectric Stiffening and occurs due to the electromechanical coupling. The expression for the new stiffness constant can be written as

$$c'_{55} = c_{55} (1 + K^2) \quad (3-27)$$

where

$$K^2 = \frac{e_{x5}^2}{c_{55}\epsilon_{xx}} \quad (3-28)$$

K^2 is the electromechanical coupling coefficient, which defines the strength of the electromechanical coupling effect.

3.4 Finite Element Formulation

As mentioned earlier the finite element formulation of piezoelectric constitutive relations has been well developed and understood in the literature. The following is a brief outline of the procedure.

The piezoelectric constitutive equations have been clearly stated above (3-18). The degrees of freedom are the nodal displacements in x , y and z directions and voltage. Evaluation of the voltage and displacement within the element, U_c and V_c respectively are derived using the element shape functions;

$$\begin{aligned}
U_c &= \{N^u\}^T (U) \\
V_c &= \{N^v\}^T (V)
\end{aligned}
\tag{3-29}$$

The coupled finite element matrix equation for a one element model is [30]

$$\begin{bmatrix} [M] & [0] \\ [0] & [0] \end{bmatrix} \begin{Bmatrix} \ddot{u} \\ \ddot{v} \end{Bmatrix} + \begin{bmatrix} [C] & [0] \\ [0] & [0] \end{bmatrix} \begin{Bmatrix} \dot{u} \\ \dot{v} \end{Bmatrix} + \begin{bmatrix} [K] & [K^z] \\ [K^z]^T & [K^d] \end{bmatrix} \begin{Bmatrix} u \\ v \end{Bmatrix} = \begin{Bmatrix} F \\ L \end{Bmatrix}
\tag{3-30}$$

F is the vector of nodal forces and L is the vector of nodal electric charge. The sub-matrices are defined as [30]

$$\begin{aligned}
[M] &= \int_{vol} \rho [N^u] [N^u]^T dv \\
[K] &= \int_{vol} [B_u]^T [c] [B_u] dv \\
[K^d] &= - \int_{vol} [B_v]^T [\varepsilon] [B_v] dv \\
[K^z] &= \int_{vol} [B_u]^T [e] [B_v] dv
\end{aligned}
\tag{3-31}$$

$[M]$ is the structural mass matrix, $[K]$ is the structural stiffness matrix, $[K^d]$ is the dielectric permittivity matrix and the $[K^z]$ is the Piezoelectric coupling matrix. To have a better understanding of B_u and B_v , it is crucial to define the strain and electric fields as;

$$\begin{aligned}
[S] &= [B_u] \{u\} \\
[E] &= -[B_v] \{v\}
\end{aligned}
\tag{3-32}$$

$[B_u]$ is a gradient operator matrix and $[B_v]$ is the gradient vector.

ANSYS® solves the equilibrium equations using the Newmark method [30]. The method is conditionally stable if the integration parameters and the time step have the satisfy the following conditions[31]:

$$\gamma \geq \frac{1}{2}, \quad \beta \leq \frac{1}{2} \quad \text{and} \quad \Delta t \leq \frac{1}{\omega_{max} \sqrt{\gamma/2 - \beta}}
\tag{3-33}$$

and unconditionally stable if [31]

$$2\beta \geq \gamma \geq \frac{1}{2} \quad (3-34)$$

These limiting factors for β and γ are set in ANSYS® when carrying out the simulations in this study.

3.5 Interdigital Transducers (IDT)

White [3] discovered that Surface Acoustic Waves can be launched and detected using interdigital (*finger-like*) electrodes patterned on the surface of a piezoelectric substrate (hence the name Interdigital Transducer) using lithographic techniques. Applying a time varying voltage signal across the electrodes generates an electric field. A strain field is simultaneously created in the crystal due to the *Converse* piezoelectric effect and a mechanical wave propagates along the surface of the piezoelectric crystal. The mechanical wave is detected as a voltage output at the receiver due to the *Direct* piezoelectric effect.

The overall transfer function $H(f)$ of the device is a product of the transfer functions of the input and output transducers, shown in (3-35). The phase delay term corresponds to the distance (d) between the centers of both IDT's, referred to as the center-to-center distance.

$$H(f) = \frac{V_{out}}{V_{in}} = H_{in}(f)H_{out}(f)e^{-jkd} \quad (3-35)$$

3.5.1 Delta Function Model

This model approximates the electric field distribution between adjacent electrodes of an excited IDT. It gives the relative insertion loss since it does not take into consideration the impedance level and second order effects. However, it provides a basic understanding of the response of SAW devices operated by interdigital transducers.

When a voltage signal is applied to an IDT there is an instantaneous charge accumulation at the electrodes. The resultant charge distribution is represented as

discrete *Delta* function sources with electric field intensity E_y . The magnitude of the Delta functions is proportional to the amplitude of the applied voltage signal. Figure 3 illustrates the alternating polarities of the Delta sources on the electrode surface of an excited IDT.

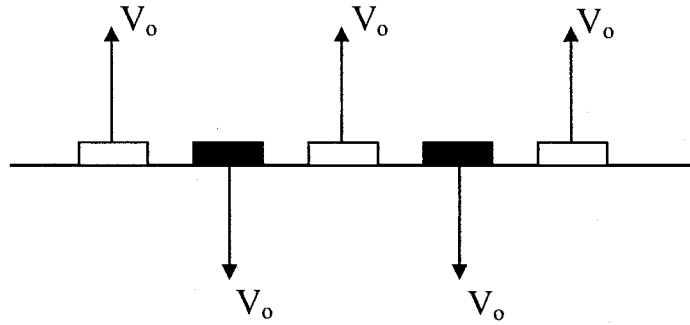


Figure 3: Delta Sources on Electrodes of IDT

Summation of the Delta sources generates the response of the IDT and is used to derive its transfer function [4];

$$H(f) = \sum_{n=-(N_f-1)/2}^{(N_f-1)/2} (-1)^n V_o e^{-jnkp/2} \quad (3-36)$$

where N_f is the number of fingers of the IDT, k is the wave number and p is the distance between two similarly charged electrodes. This summation is a geometric series whose elements are 1 and add constructively when $\frac{kp}{2} = m\pi$, where m is an odd integer. The response of the IDT-SAW device is illustrated in Figure 4.

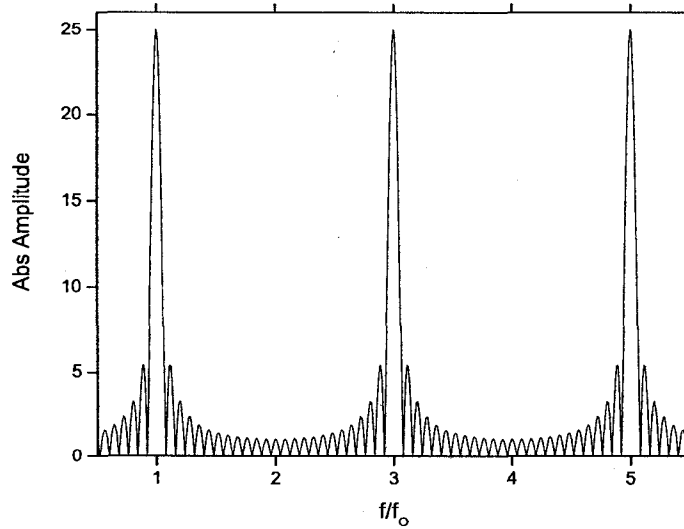


Figure 4 Response of IDT-SAW Device in Delta Function Model

The IDT operates most efficiently when the distance between two similarly charged electrodes p is an odd multiple of the wavelength λ , therefore it will excite odd harmonics of the center frequency.

The geometric series can be approximated by [15];

$$|H(f)| = N_p \left| \frac{\text{Sin}(X)}{X} \right| \quad (3-37)$$

where;

$$X = N_p \pi \left(\frac{f - f_0}{f_0} \right)$$

N_p is the number of electrode pairs of the IDT and f_0 is the center frequency.

3.6 Surface Acoustic Wave Perturbation Mechanisms

The SAW propagates along the surface and its energy is confined within a depth of a few wavelengths from the surface, therefore any change in the surrounding environment will affect the SAW propagation. The parameter of the SAW used to detect changes in the surroundings is the phase velocity. The phase velocity v_o is defined as “the propagation velocity of a point of constant phase” [27]. The phase

velocity is proportional to the material properties of the medium in which it propagates:

$$v_o = \sqrt{\frac{c}{\rho}} \quad (3-38)$$

where c is the stiffness constant (N/m^2) and ρ is the density (kg/m^3).

The phase velocity of the SAW is related to changes in the surrounding environment as follows [32]:

$$\frac{\Delta v}{v_o} = \frac{1}{v_o} \left[\frac{\partial v}{\partial m} \Delta m + \frac{\partial v}{\partial c} \Delta c + \frac{\partial v}{\partial T} \Delta T + \frac{\partial v}{\partial p} \Delta p + \frac{\partial v}{\partial \varepsilon} \Delta \varepsilon + \frac{\partial v}{\partial \sigma} \Delta \sigma + \frac{\partial v}{\partial \mu} \Delta \mu + \dots \right] \quad (3-39)$$

where v_o is the SAW velocity, m is mass, c is stiffness, T is temperature, p is pressure, ε is dielectric constant, σ is conductivity, μ is viscosity. In order to determine the affect of any one of these parameters on the wave velocity a Perturbation approach is often used [28].

3.6.1 Velocity and Attenuation Changes

Velocity and attenuation changes are related to changes in the energy density and power dissipation respectively. For illustrative purposes consider a wave with a power density (power/beam width) P passing through a unit cube. The energy density of the cube increases by $U = P\tau$, where τ is the time it takes the wave to traverse the unit cube i.e. $\tau = \frac{1}{v}$, where v is the wave velocity [4]. The power density of the wave can be written as;

$$P = Uv \quad (3-40)$$

Implicit differentiation of ((3-40) in a lossless medium i.e. at constant P yields [4]

$$\frac{\Delta v}{v_o} = -\frac{\Delta U}{U_o} \quad (3-41)$$

This illustrates the relation between changes in wave velocity and energy density. The Energy conservation principle (also known as Rayleigh Conservation Principle)

states that “in a lossless medium the peak strain energy density must equal the peak kinetic energy density” [4]. When a wave is excited at a given frequency in a medium the change in velocity can be thought of as the change the wavelength undergoes to maintain the kinetic and strain energies equal.

For a wave propagating in a lossy medium the Power density (P) of the wave is represented by [4]

$$P(x) = P_0 e^{-2\alpha x} \quad (3-42)$$

α is the attenuation. The dissipated power (power/volume) is related to power density by

$$P_d = -\frac{\partial P}{\partial x} \quad (3-43)$$

Therefore P_d can be expressed as

$$P_d = 2\alpha P \quad (3-44)$$

where the attenuation α is

$$\alpha = \frac{P_d}{2P} \quad (3-45)$$

Therefore the attenuation can be interpreted as the ratio of the power dissipated to the power density of the wave. For a wave propagating in the x -direction of a lossy medium, the displacement field is expressed as [4]

$$u(x, y, z, t) = u_i e^{j(\omega t - kx)} \cdot e^{-\alpha x} \quad (3-46)$$

With simple algebraic manipulation the displacement field is expressed as

$$u(x, y, z, t) = u_i e^{j\omega t - \gamma x} \quad (3-47)$$

where

$$\gamma = \alpha + jk \quad (3-48)$$

γ is the complex propagation factor that represents both attenuation and the wave number. Changes in wave propagation can therefore be represented by [4]

$$\Delta\gamma = \Delta\alpha - jk_o \frac{\Delta v}{v_o} \quad (3-49)$$

in normalized form

$$\Delta\gamma' = \frac{\Delta\alpha}{k_o} - j \frac{\Delta v}{v_o} \quad (3-50)$$

which represents the general perturbation to wave propagation that affects both the wave velocity and attenuation. As mentioned earlier the changes in wave velocity and attenuation are related to changes in energy density and power dissipation respectively. The derivative of the change in energy density and the power dissipation can be grouped into a single term referred to as the Complex Power Transfer (P_T) from the wave [4];

$$P_T = P_d + j2\omega(\Delta U) \quad (3-51)$$

therefore the changes in the complex propagation factor can be related to the complex power transfer from the wave to give the general relationship;

$$\Delta\gamma' = \frac{\Delta\alpha}{k_o} - j \frac{\Delta v}{v_o} = \frac{P_T}{2k_o P} \quad (3-52)$$

The form of the complex power transfer term varies according to the perturbing factor.

Chapter 4

4 A 3D Surface Acoustic Wave Sensor Model for Hydrogen Detection

4.1 Introduction

Hydrogen plays a significant role in various industrial applications such as the preparation of ammonia and methanol, the hydrogenation of organic compounds and in the production of semiconductors. In addition, it is used in the reduction of iron ores to metallic iron, in petroleum recovery and refining and acts as a cooling medium for high speed turbines in power generation. Moreover, it is used in fueling spacecrafts and is used in fuel cells to power consumer electronic devices. Also there are applications of hydrogen fueled internal combustion engines, gas turbines and reciprocating engines. However, when using hydrogen careful handling is crucial. Hydrogen diffusion into metals causes embrittlement, cracks and degradation in material properties which can cause catastrophic failure. In addition, hydrogen is explosive when mixed with air at a minimum ratio of 4% [33]. Due to its wide applications and mishandling hazards careful monitoring of hydrogen leakage is crucial.

4.2 Hydrogen Sensing Mechanisms

Hydrogen sensors based on various sensing mechanisms have been developed for quite some time. A brief description of various hydrogen sensing mechanisms is presented with some examples from the literature.

4.2.1 Pyroelectric Gas Analyzers (PGA)

Pyroelectricity is a physical property where materials become electrically polarized due to temperature variation. A change in temperature causes dimensional

changes in a pyroelectric material, which induces changes in the surface charge density. This effect produces a potential difference across the surfaces of the material.

D'amico and Zemel [34] used a 300 μm thick Lithium Tantalate (LiTaO_3) wafer, a pyroelectric material and covered it with Gold and Palladium electrodes on the top surface and another Gold electrode on the bottom surface. When Hydrogen gas is introduced it is absorbed by the Palladium electrode. This reaction causes heat generation at the Palladium electrode and hence leads to a change in the voltage signal. The Gold electrode on the top surface undergoes no chemical reaction and hence is used as a reference electrode. The difference in voltage between the two signals is an indicator of Hydrogen absorption.

4.2.2 Fiber Optic Sensors (FOS)

Fiber optics are waveguides that allow light to travel at optical frequencies. The operating principle of FOS in gas detection is simple. The optical fiber is coated with a thin layer of a chemically selective film. The absorption of gas molecules by the film induces changes in the optical fiber that affect the properties of the beam.

Butler [35] used Palladium coated quartz fibers for Hydrogen detection. A 1 μm thick Palladium film was sputtered on the quartz fiber. The beam from the Laser source was split in two directions; one to travel through the Palladium coated fiber and the other for the uncoated reference fiber. Both fibers were subjected to Hydrogen flow and the beam properties were recorded. The Palladium coated fiber expanded due to Hydrogen absorption, this expansion stretched the fiber in both the radial and axial directions and hence changed the effective optical length. The change in optical length leads to a phase shift in the beam when compared with the reference fiber.

4.2.3 Electrochemical Sensors

The electrochemical sensor consists of two electrodes immersed in an electrolyte that acts as the transferring medium for ions between the sensing electrode and the reference electrode. Kumar [36] used an electrochemical cell with a solid electrolyte

for Hydrogen detection. The sensing electrode was Platinum (Pt) and the reference electrode was Lead Oxide (PbO₂). Hydrogen gas was introduced at various concentrations. The Pt electrode reacted with Hydrogen and produced Hydrogen protons that were transferred through the electrolyte to the reference electrode thus creating an abundance of electrons at the Pt electrode. A current normally flows through the external circuitry and can be used as a measure of the hydrogen concentration, however, in this application the potential difference between the two electrodes was measured.

4.2.4 Quartz Crystal Microbalance (QCM)

The operating principle of the QCM is illustrated in the Literature Review Chapter. In this section applications of the QCM in Hydrogen detection is presented.

Łukaszewski [37] used QCM's coated with several gas sensing films of Pure Pd and Pd alloys for hydrogen detection. The frequency shifts for the various sensing films were recorded at different hydrogen concentrations. It was found that the results were higher than the expected theoretical values. The reason for the discrepancy was that induced stresses during hydrogen absorption contributed to the frequency shifts. Frazier [38] used a Pd coated QCM to determine the Phase Diagram of the Palladium Hydrogen system. The Pd coated QCM was placed in a chamber where hydrogen gas was added and the pressure was incrementally increased. Frequency shifts corresponding to hydrogen absorption were recorded for the pressure range applied. The process was repeated for different temperatures. The results were in agreement with the Phase Diagrams in the literature.

QCM and SAW sensors have closely related operating principles, however SAW sensors offer higher sensitivity because they can operate at much higher frequencies [39]. As the operating frequency of SAW sensors increases the wave is more confined near the surface and becomes more sensitive to changes in the adjacent environment.

In this study a YZ Lithium Niobate SAW sensor with a thin Pd film on the surface is used for Hydrogen detection.

4.3 The Hydrogen Palladium System

Hydrogen has high solubility in many transition metals. The Hydrogen Palladium system has been one of the most experimentally investigated since Graham [40] observed that large volumes of Hydrogen were absorbed or as he termed it *Occluded* by Palladium during Electrolysis. Many of the sensors developed for Hydrogen detection use Palladium as an intermediate selective layer as illustrated above.

Volume dilatation of the palladium lattice due to the Hydrogen absorption induces lattice strains. Baranowski [41] showed that for different fcc metals and alloys the increase in volume of the unit cell due to interstitial Hydrogen is linear up to a concentration $c = 0.75$ then the slope changes. A hydride stoichiometry of $c = 1$ can be achieved where the Hydrogen atoms occupy all the octahedral sites of the Pd lattice and the ideal Sodium Chloride structure is achieved [42].

When Palladium absorbs n Hydrogen atoms its volume V changes by $\Delta V = n\Delta v$, where Δv is the change in volume per Hydrogen atom. If the mean atomic volume of a Palladium atom is Ω , then $V = N\Omega$. The relative volume change due to an atomic fraction $c = n/N$ is $\Delta V/V = c(\Delta v/\Omega)$, which is related to the lattice expansion approximately by $c(\Delta v/\Omega) = 3(\Delta a/a)$, where a is the lattice constant [43]. The results of various experiments for the relative volume change due to Hydrogen absorption are collected in Peisl [43]. Almost all of the experiments were carried out at room temperature and a value for the relative volume change $\Delta v/\Omega$ of 0.19 ± 0.01 was obtained. In this study the value of 0.19 for the relative volume change will be used. At different Hydrogen concentrations the corresponding density ρ_c of Palladium is calculated using [44];

$$\rho_c = \left(\frac{1 + \frac{m_H}{m_{Pd}} c}{1 + 3 \frac{\Delta a}{a} c} \right) \rho_o \quad (4-1)$$

where the molar masses m_H and m_{Pd} are 1.008 g/mol and 106.42 g/mol [45], respectively and ρ_o is density of pure Pd. In addition to the change in density the lattice expansion reduces the elastic constants of Palladium as will be illustrated.

4.4 Finite Element Modeling of a SAW-IDT Sensor

A finite element model of a SAW Sensor was developed using ANSYS® 11.0. The objective at this stage is to build a model and ensure it works correctly. The sensor is a layered piezoelectric substrate with interdigital transducers at the interface. The piezoelectric substrate used is XY-Lithium Niobate (LiNbO_3). The coordinate axis is rotated such that the X-crystal axis is perpendicular to the substrate surface and the Y-crystal axis parallel, hence defining the XY- LiNbO_3 crystal. The Y-crystal axis is the direction of wave propagation. The surface of the XY- LiNbO_3 substrate is completely covered with a thin piezoelectric Zinc Oxide (ZnO) film. A schematic of the device layout with dimensions is presented in Figure 5.

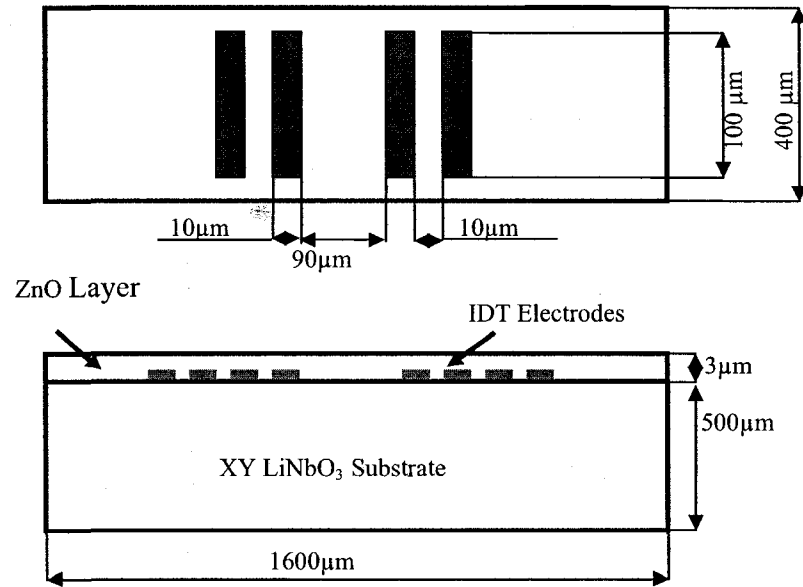


Figure 5: Schematic of XY- LiNbO_3 ZnO Device Layout

The parameters used in this model are a replication of the parameters used by Ippolito *et al* [21] who provides both simulation and experimental results. The output

of the model was compared with the published results for verification. The sensor parameters are listed in Table 2.

The electrodes were modeled as a set of nodes coupled by a voltage degree of freedom. The electrode mass has a negligible affect on the results of the adopted configuration [21, 23, 25]. Xu [26] studied the effect of electrode mass on sensor response using Finite Element analysis. The electrode mass caused the center frequency to drift to a lower value and the insertion loss to increase when the center frequency was in the range of 1GHz. The results indicate that the interference due to the electrode mass is significant for devices operating at such a high center frequency (above 1GHz) and can be neglected in these cases. The operating frequency of the XY-LiNbO₃ ZnO model is in the range of 100MHz.

Table 2: Parameters for XY-LiNbO₃ ZnO Sensor

<i>Parameters</i>	<i>Value</i>
<i>XY-LiNbO₃ Substrate Dimensions</i>	<i>1600x500x400μm</i>
<i>Number of Electrode Pairs for each IDT</i>	<i>2</i>
<i>Propagation Distance</i>	<i>90μm</i>
<i>Electrode width and Spacing</i>	<i>10μm</i>
<i>Wavelength (λ)</i>	<i>40μm</i>
<i>Electrode Length</i>	<i>100μm</i>
<i>Thickness of ZnO Layer</i>	<i>3μm</i>

The material properties of Lithium Niobate are listed in Table 3. The density of Lithium Niobate is 4,647 kg/m³. The material properties are been obtained from Wong [46].

Table 3: Material Properties for Lithium Niobate

Elastic Matrix In Stiffness Form ($\times 10^{11}$ Pa)		Piezoelectric Matrix at Constant Strain(C/m^2)		Permittivity Matrix at Constant Strain ($\times 10^{-11}$ F/m)	
C_{11}	2.03	e_{15}	3.7	ϵ_{11}	39
C_{12}	0.573	e_{22}	2.5	ϵ_{33}	20.4
C_{13}	0.752	e_{31}	0.2		
C_{14}	0.085	e_{33}	1.3		
C_{33}	2.424				
C_{44}	0.595				
C_{66}	$\frac{C_{11} - C_{12}}{2} = 0.7285$				

The material properties of Zinc Oxide are listed in Table 4. The Density of ZnO is $5,720 \text{ kg/m}^3$. The material properties are obtained from Didenko [47].

Table 4: Material Properties for Zinc Oxide

Elastic Matrix In Stiffness Form ($\times 10^{11}$ Pa)		Piezoelectric Matrix at Constant Strain(C/m^2)		Permittivity Matrix at Constant Strain ($\times 10^{-11}$ F/m)	
C_{11}	1.57	e_{15}	-0.45	ϵ_{11}	7.35
C_{12}	0.89	e_{31}	-0.51	ϵ_{33}	7.79
C_{13}	0.83	e_{33}	1.22		
C_{33}	2.08				
C_{44}	0.38				
C_{66}	$\frac{C_{11} - C_{12}}{2} = 0.34$				

Lithium Niobate and Zinc Oxide are piezoelectric materials, therefore the same element type was used in meshing both volumes. The Solid226 3D Coupled Field Solid element was selected. The element adopts Structural-Thermal, Piezoresistive, Electroelastic, Piezoelectric, Thermal-Electric, Structural-Thermoelectric and Thermal-Piezoelectric capabilities [48]. The element has up to five degrees of freedom per node. The tetrahedron geometrical configuration was adopted. The key-options of the element were set to allow three structural degrees of freedom per node; U_x , U_y and U_z and one electrical degree of freedom; Voltage (V).

4.4.1 Boundary Conditions

The boundary conditions on the model are stated below and illustrated in Figure 6.

- Clamped condition on the bottom surface A_1

$$(u_x, u_y, u_z, \phi = 0)$$

to fix the sensor in place and reduce second order effects [15].

- Continuity of the displacement field components U_i for $i = x, y, z$ and the voltage ϕ at interface I
- A Traction free boundary at the Free Surface S

$$T_{iz} = 0 ; \text{ for } i = x, y, z$$

- The following Dirichlet conditions for the electric potential

$$\begin{aligned}\phi|_{R1} &= 0 \\ \phi|_{R2} &= V(t) \\ \phi|_{R3} &= O(t)\end{aligned}$$

where $V(t)$ is the input voltage signal and $O(t)$ is the voltage response at the output electrodes. The condition for $\phi|_{R1}$ is achieved by selecting the nodes corresponding to the electrode region and setting their voltage DOF to Zero. For $\phi|_{R2}$ all input electrodes are coupled together with a volt DOF and the input signal is applied to the primary node. Each output electrode corresponding to R_3 is coupled separately. The voltages at the primary nodes in the output electrodes are added together to determine the sensor response.

- Extension of the boundaries B_1 and B_2 along the length direction as indicated by the arrows and the same for the width boundaries W_1 and W_2 . This condition is necessary to avoid wave reflections from the boundaries that would cause interference and hence deteriorate the response.

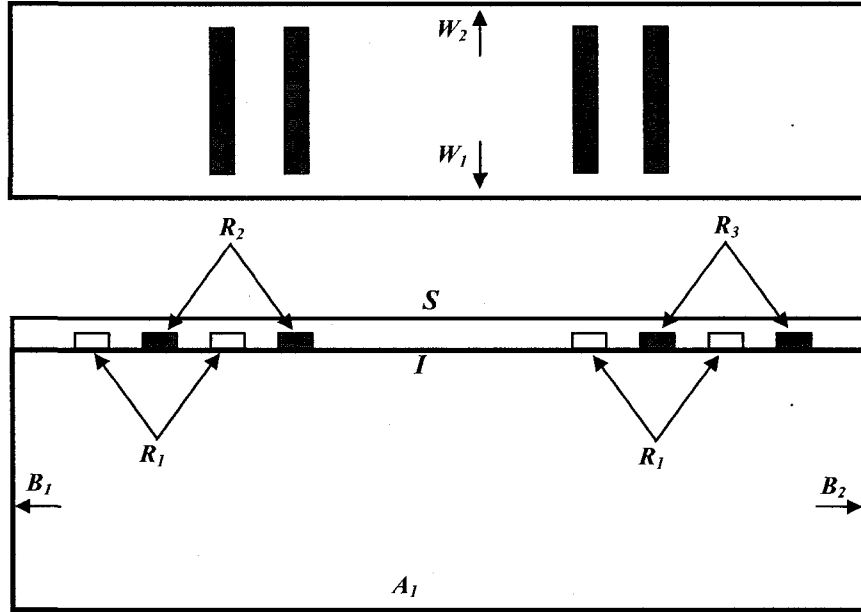


Figure 6: Boundary Conditions Representation

Table 5 summarizes the boundary conditions in the XY-LiNbO₃ ZnO model. This device layout is the most general layout used in this study. The boundary conditions in other models that will be built in this study are variations of those in XY-LiNbO₃ ZnO. Comparisons will be made to illustrate the variations that take place as the device layout changes. A tick ✓ implies that the boundary condition applies in the corresponding model, meanwhile a cross ✗ implies that the boundary condition does not apply.

Table 5: Boundary Condition Table for XY-LiNbO₃ ZnO Model

Boundary Conditions		XY-LiNbO ₃ ZnO Model
Clamped Condition on A ₁	$(u_x, u_y, u_z, \phi = 0)$	✓
Dirichlet Conditions	$\phi _{R1} = 0$ $\phi _{R2} = V(t)$ $\phi _{R3} = 0(t)$	✓
Continuity of the Displacement field at Interface I	U_i for $i = x, y, z$	✓
Continuity of the Voltage at Interface I	ϕ	✓
Traction Free Boundary at S	$T_{iz} = 0$; for $i = x, y, z$	✓
Extension of Boundaries	B_1, B_2, W_1 & W_2	✓

4.4.2 Transient Analysis

The FE model of the SAW sensor is shown in Figure 7. A transient analysis is performed where an impulse signal is applied to the input electrodes. The applied signal is illustrated in (4-2) where T_s is the time step size. The simulation was run for 100ns with $T_s = 1ns$.

$$V_{in} = \begin{cases} 1 \times 10^9 & \text{for } 0 < t \leq T_s \\ 0 & \text{for } t > T_s \end{cases} \quad (4-2)$$

The objective is to determine the frequency response of the sensor, which is obtained from the Fourier Transform of the Impulse response. A 512pt-FFT code was developed in Matlab® and the frequency response of the sensor was determined. The Insertion Loss IL(dB) in the sensor was calculated using

$$IL(dB) = 20 \text{Log}_{10} \left(\frac{V_{out}}{V_{in}} \right) \quad (4-3)$$

where V_{out} is the magnitude of the voltage at various frequencies in the frequency response and V_{in} is the magnitude of the input voltage.

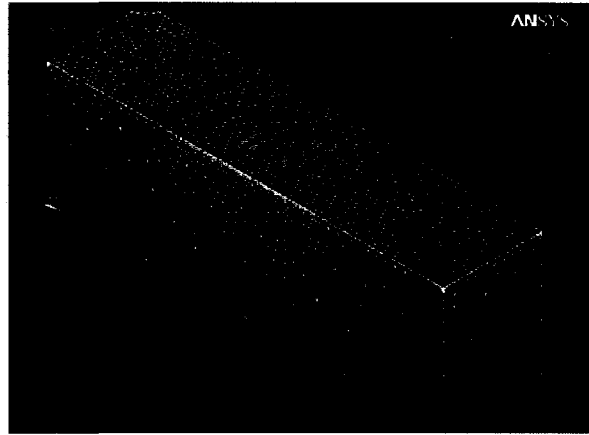


Figure 7: FE Model of XY-LiNbO₃ ZnO SAW Sensor

The elements at the interface of the XY-LiNbO₃ substrate and the ZnO film were refined to obtain the most accurate center frequency value. The goal was to increase the number of elements per wavelength to ensure the wave was fully captured. The element size data are listed in Table 6. Figure 8 illustrates the mesh convergence.

Table 6: Different Element Sizes for XY-LiNbO₃ ZnO Model

<i>ESIZE</i> (μm)	<i>Elem</i> / λ $\lambda=40(\mu\text{m})$	f_c	<i>%Error</i>
12	3.33	100.56	0.56
15	2.67	101.6	1.6
18	2.22	103.52	3.52
21	1.9	105.47	5.47
25	1.6	112.3	12.3

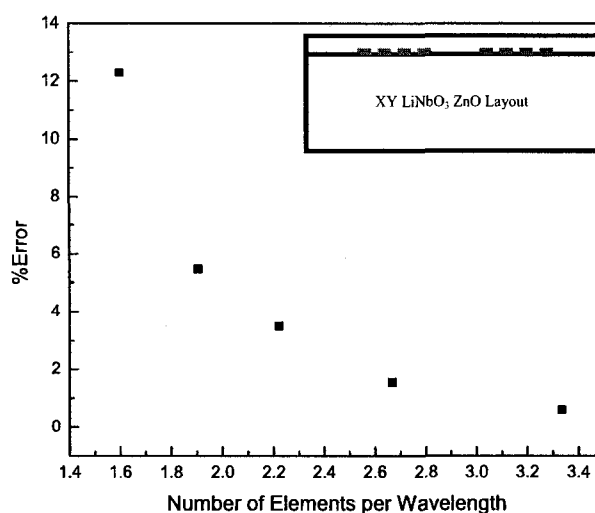


Figure 8: Mesh Sensitivity Analysis for XY-LiNbO₃ ZnO Model

Figure 9 shows the comparison between the response obtained using the current simulation and the experimental and simulation results published by Ippolito *et al* [21]. The plot illustrates the IL(dB) of the sensor in the region 70-130MHz. The SAW velocity in this configuration is 4,000m/s [21]. The wavelength was set to 40 μm as mentioned in Table 2. The center frequency can be calculated from $f_c = v/\lambda$. In this case f_c is expected to be 100MHz. In our model the closest value is $f_c=100.56\text{MHz}$. The center frequency in the experimental data shown in Figure 9 is 103MHz. The

3MHz variation in the experimental results is due to the tolerance involved in fabricating the electrodes.

The target in comparing the simulation results with the published results is matching the center frequencies. The current simulation appears to agree with the experimental results more accurately than the simulation published by Ippolito *et al* [21]. The Insertion Loss value in the current simulation is -35.5dB in comparison with -34.3dB in the experimental data. Table 7 lists the Frequency and Insertion Loss results. However, there is a major discrepancy at 93MHz between both simulation results and the experimental. This is due to the few number of electrodes used, which leads to a broad bandwidth and therefore causes spurious oscillations and instability in the circuit as seen in the experimental results [4].

Table 7: Comparison of Simulation Results with Published Results

	<i>Center Frequency (MHz)</i>	<i>IL(dB)</i>
<i>Experimental [21]</i>	<i>103</i>	<i>-34.3</i>
<i>Simulation [21]</i>	<i>100</i>	<i>-37.5</i>
<i>Our Simulation</i>	<i>101.56</i>	<i>-35.5</i>

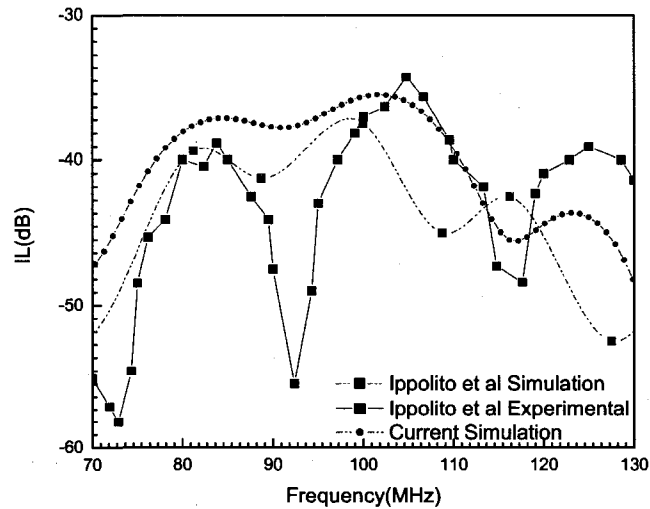


Figure 9: Verification of Simulation Results for XY-LiNbO₃ ZnO Model

4.5 SAW Model for H₂ Absorption

The model used for Hydrogen detection is different than the model used for verification. The new model consists of a YZ-LiNbO₃ bare substrate with a thin Palladium film deposited on the propagation path for hydrogen absorption as illustrated in Figure 10. This orientation of LiNbO₃ is widely used for SAW sensors and its properties are very well established in the literature.

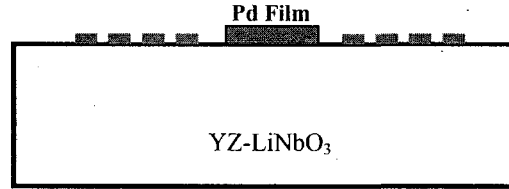


Figure 10: Layout of YZ-LiNbO₃ SAW Device with Thin Pd Film

In this case a Transient analysis is performed, where an impulse signal is applied to the model and the frequency response is obtained by the Fourier Transform of the impulse response. Hydrogen absorption changes the material properties of the Pd film as will be shown, which affects the wave velocity. The velocity of the wave for the different cases will be measured and used to assess the sensor response.

The velocity is obtained from the Phase value at the center frequency. The phase is related to the velocity in the following way;

$$\phi = -\omega \cdot T_o = -\omega \cdot \frac{l}{v} \quad (4-4)$$

where ω is the angular frequency, T_o is the time it takes the wave to travel a given distance l and v is the velocity of the wave. In addition,

$$\Delta\phi = \omega \cdot \frac{l}{v^2} \Delta v \quad (4-5)$$

therefore,

$$\left| \frac{\Delta\phi}{\phi} \right| = \left| \frac{\Delta v}{v} \right| \quad (4-6)$$

(4-6) will be used to determine the change in velocity for the different cases of Hydrogen absorption. All changes in phase will be calculated with respect to the Pure Pd case.

4.5.1 YZ-LiNbO₃ SAW Model

The material properties of Lithium Niobate listed in Table 3 are used. The element coordinate system is rotated such that the Y-crystal axis is perpendicular to the device surface and the Z-crystal axis is parallel to the substrate surface and is the direction of propagation. The Lithium Niobate substrate was meshed with Solid226 3D Coupled Field Solid element, with four DOF per node; displacements U_x , U_y and U_z and Voltage (V).

The boundary conditions are different than in the XY-LiNbO₃ ZnO model. When modeling the Palladium film continuity of the displacement field is imposed at the film-substrate interface and a stress free boundary condition is applied at the Pd free surface. A stress free boundary is also applied to the region outside the IDT's on the YZ-LiNbO₃ substrate. The set of boundary conditions is illustrated in Table 8.

Table 8: Boundary Condition Table for YZ-LiNbO₃ Model

Boundary Conditions		XY-LiNbO₃ ZnO Model	YZ-LiNbO₃ Model
Clamped Condition on A_1	$(u_x, u_y, u_z, \phi = 0)$	✓	✓
Dirichlet Conditions	$\phi _{R1} = 0$ $\phi _{R2} = V(t)$ $\phi _{R3} = O(t)$	✓	✓
Continuity of the Displacement field at Interface I ^(a)	U_i for $i = x, y, z$	✓	✓
Continuity of the Voltage at Interface I	ϕ	✓	✗
Traction Free Boundary at S	$T_{iz} = 0$; for $i = x, y, z$	✓	✓
Extension of Boundaries	B_1, B_2, W_1 & W_2	✓	✓

A mesh sensitivity analysis was carried out to determine the optimum number of elements along the wavelength that fully capture the wave. The elements in the region of wave propagation are refined. The refinement decreases with increasing depth into the substrate. The parameters of the model used in this analysis are listed in Table 9. The convergence criterion was the center frequency. The wave velocity of a SAW on a YZ-LiNbO₃ substrate is 3,488m/s [25]. The impulse signal in (4-2) was applied and the simulation was run for 400ns.

Table 9: Parameters for YZ-LiNbO₃ SAW Sensor

<i>Sensor Parameter</i>	<i>Parameter Value</i>
<i>Substrate Dimensions</i>	<i>3500x400x500μm</i>
<i>Number of Electrode Pairs for each IDT</i>	<i>12</i>
<i>Wavelength (λ)</i>	<i>34.88μm</i>
<i>Electrode width and Spacing between the electrodes</i>	<i>$\lambda/4$</i>
<i>Propagation Distance</i>	<i>523.2μm</i>
<i>Electrode Length</i>	<i>200μm</i>

The target center frequency is 100MHz. The frequency in each case was determined from the frequency response of the sensor. The %Error was calculated to determine if convergence was reached.

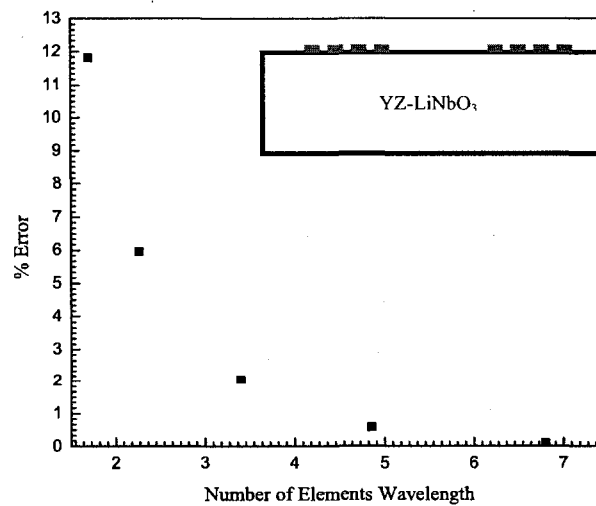


Figure 11: Mesh Sensitivity Analysis for YZ-LiNbO₃ Model

After achieving mesh convergence trial runs were held in an attempt to increase the operating frequency for better sensitivity. The limiting factor was the number of elements. As the operating frequency increases the wavelength decreases thus requiring more elements in the model to ensure the wave is fully captured. The highest frequency value that could be reached was 130MHz. The element size adopted for the 130MHz was reduced further than the sizes used in the 100MHz mesh sensitivity analysis. The element size was set to allow almost four elements per wavelength. The corresponding center frequency was 127.44MHz giving a Error of 1.9%.

The boundaries B_1 and B_2 have been extended to eliminate any reflections that could deteriorate the signal response in the analysis. Initially the length of the substrate was set to a minimal value such that the edges were very close to the input and output IDT's. This initial length is denoted as L_o . Multiples of L_o were used to determine the change in sensor response.

Figure 12 and Figure 13 illustrate the center frequency and the IL values corresponding to the different values of L / L_o respectively. It can be clearly seen that the effect of substrate length on the sensor response is negligible. The frequency values varied between 126-128MHz and the Insertion Loss values varied between -31 to -32dB. The reason for minimal variance is that the magnitude of the signal is high due to the large number of electrodes selected. Reflections from the boundaries were too weak to influence the sensor response.

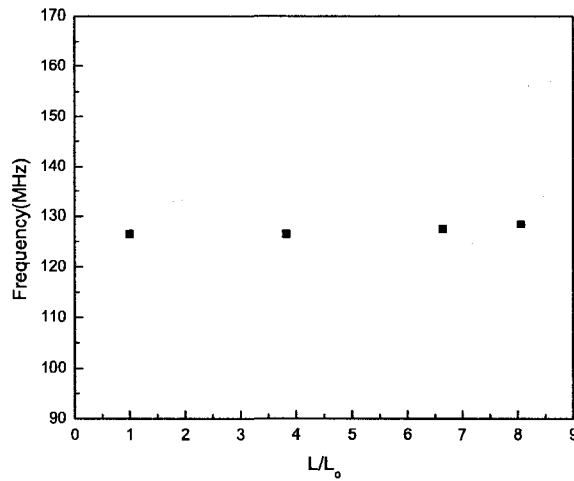


Figure 12: Effect of Substrate Length on Center Frequency of YZ-LiNbO₃ Model

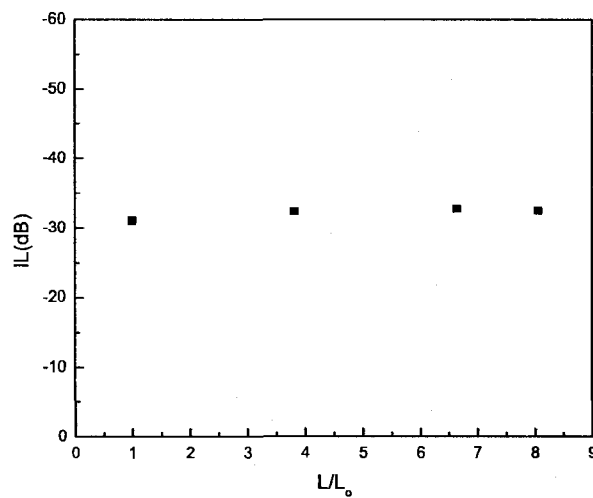


Figure 13: Effect of Substrate Length on Insertion Loss of YZ-LiNbO₃ Model

The parameters of the YZ-LiNbO₃ model operating at 130MHz are illustrated in Table 10 and the Finite Element Model of the sensor is shown in Figure 14. A Transient analysis was carried out and the impulse signal in (4-2) was applied and the simulation was run for 400ns.

Table 10: Parameters of YZ-LiNbO₃ SAW Sensor with F_c 130MHz

Sensor Parameter	Parameter Value
Substrate Dimensions	3500x400x500 μ m
Number of Electrode Pairs for each IDT	12
Wavelength (λ)	26.5 μ m
Electrode width and Spacing between the electrodes	$\lambda/4$
Propagation Distance	523.2 μ m
Electrode Length	200 μ m
Dimensions of Pd Film	423x175x2 μ m

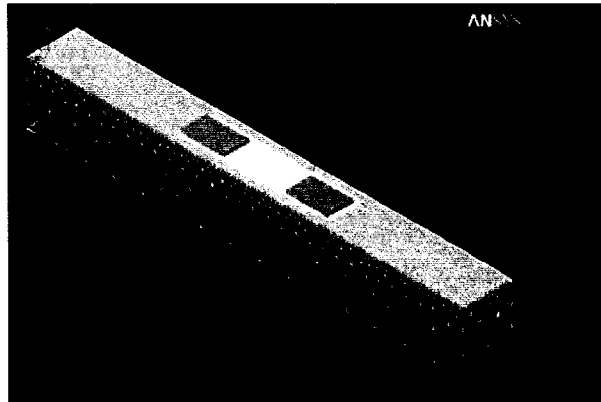


Figure 14: FE Model of YZ LiNbO₃ Sensor Operating at F_c = 130MHz

4.5.2 Modeling the Thin Palladium Film

Adding a metallic layer on the propagation path *shorts* the surface. To account for this effect the nodes at the substrate-Pd interface were coupled with a volt degree of freedom so that the voltage drop across the region of the metal film would be zero. This effect is opposite to the piezoelectric stiffening effect discussed earlier, since the short surface causes the velocity to drop back to the non-piezoelectric case.

The Palladium film was meshed with Solid98 10 node tetrahedral Coupled Field element. The element adopts Thermal, Magnetic, Electric, Piezoelectric and Structural field capabilities [48]. There are up to six degrees of Freedom per node.

The Key-options of the element were set to allow only structural degrees of freedom per node; U_x U_y and U_z .

In the literature different values for the film thickness (h) to wavelength (λ) ratio are adopted. The condition that $h < \lambda$ is mandatory. According to [32] if $h > \lambda/2$ the film can not be considered as a perturbation to the wave.

Thin Pd films exhibit a polycrystalline structure with randomly oriented crystallites, hence their structure is isotropic in the bulk [49]. The density values at different Hydrogen concentrations have been calculated using ((4-1) and the results listed in Table 11.

Due to hydrogen absorption the volume of the Palladium film increases. The increase in volume is represented only by an increase in thickness of the Pd film, therefore neglecting the shearing effects at the film-substrate interface. The Pd free surface can expand easily as it is the only unconstrained surface. The film thicknesses values adopted in the simulations are listed in Table 11. Density of Pure Pd is $12,020\text{kg/m}^3$ [44].

Table 11: Thickness of the Palladium Film at Different Hydrogen Concentrations

$c(H/Pd)$	$(\Delta V/V)$	m_H (g/mol)	m_{Pd} (g/mol)	ρ_c (kg/m^3)	Thickness [$h(\mu\text{m})$]
0	0	1.008	106.42	12020	2
0.1	0.019	1.008	106.42	12008.57	2.038
0.2	0.038	1.008	106.42	11951.94	2.076
0.3	0.057	1.008	106.42	11851.5	2.114
0.4	0.076	1.008	106.42	11709.57	2.152
0.5	0.095	1.008	106.42	11529.29	2.19

The modulus of elasticity values for polycrystalline Pd at various Hydrogen concentrations have been obtained from Fabre [44]. The Poisson's ratio for Pd can be assumed to be invariant with composition and the value for Pure Pd ($\nu=0.375$) is used [50]. For each hydrogen concentration value the corresponding modulus of elasticity

and the Poisson ratio are used to calculate the Lamé constants (c_{12} and c_{44}) [51]. The material properties adopted for Pd are listed in Table 12.

Table 12: Material Properties of Pd Thin Film

$c(H/Pd)$	E (GPa)	c_{12} (GPa)	c_{44} (GPa)	ρ_c (kg/m ³)
0	128	139.6	46.55	12020
0.1	124.5	135.8	45.27	12008.57
0.2	121.36	132.4	44.13	11951.94
0.3	118.5	129.3	43.09	11851.5
0.4	116	126.5	42.18	11709.57
0.5	113.73	124.1	41.36	11529.29

4.5.3 Results

The sensor responses to the various hydrogen concentrations are shown in Figure 15 to Figure 22. Table 13 and Table 14 summarize the results of the Insertion loss and phase data respectively. Figure 23 illustrates the change in phase near the center frequency for the various cases of Hydrogen absorption. Figure 24 shows the change in velocity at different hydrogen concentrations.

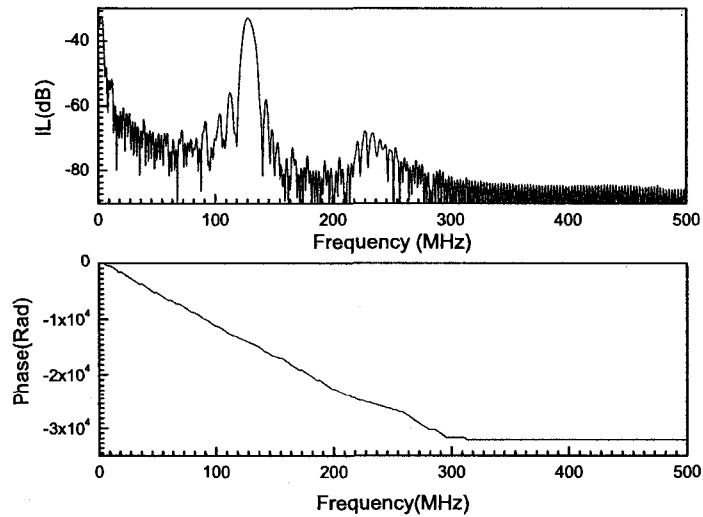


Figure 15: Frequency Response of the YZ LiNbO₃ Bare Device

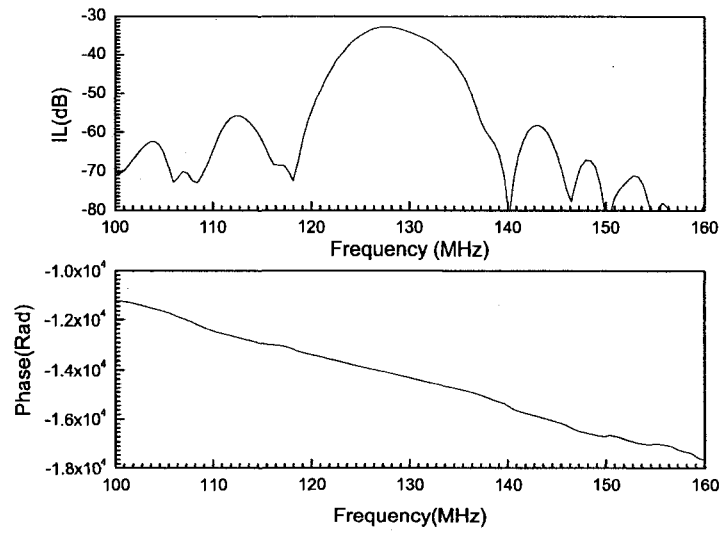


Figure 16: A Close-up on the Frequency Response of the YZ LiNbO₃ Bare Device Near $F_c=130\text{MHz}$

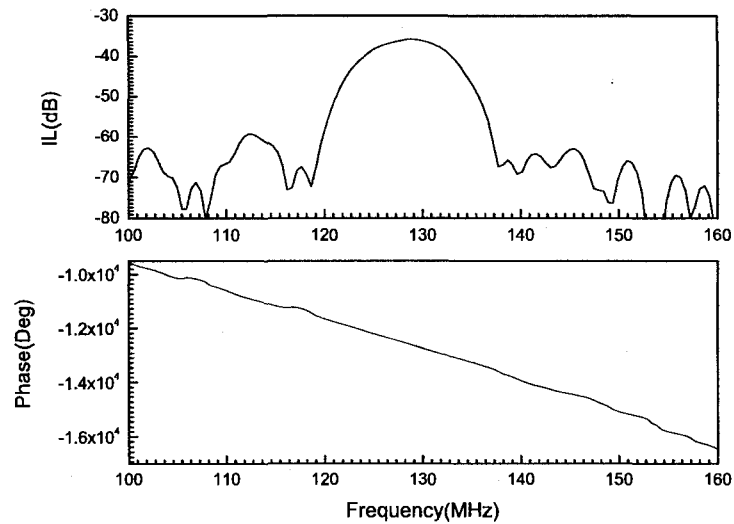


Figure 17: Frequency Response of SAW Sensor $F_c=130\text{MHz}$ with Pure Pd Film

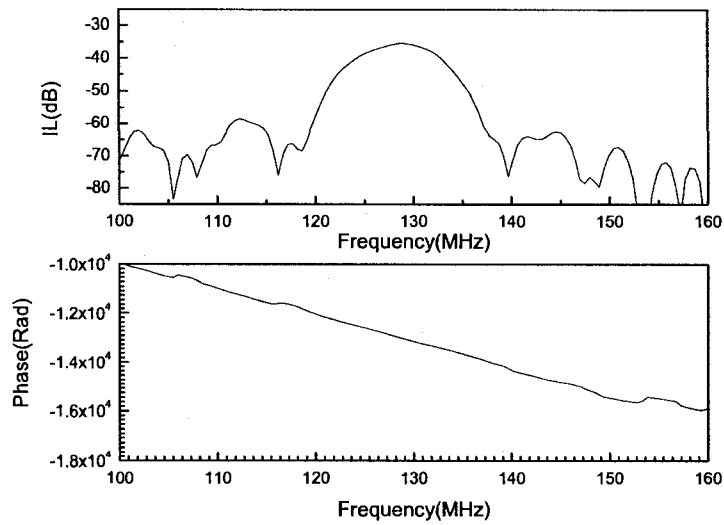


Figure 18: Frequency Response of SAW Sensor $F_c=130\text{MHz}$ with 0.1 H/Pd Concentration

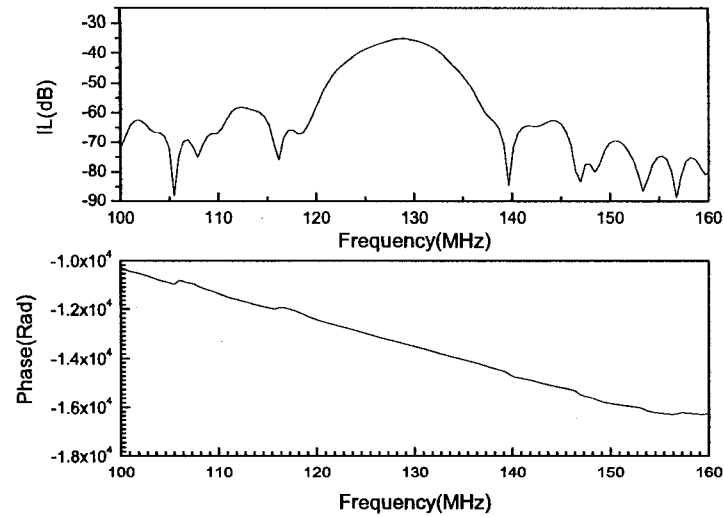


Figure 19: Frequency Response of SAW Sensor $F_c=130\text{MHz}$ with 0.2 H/Pd Concentration

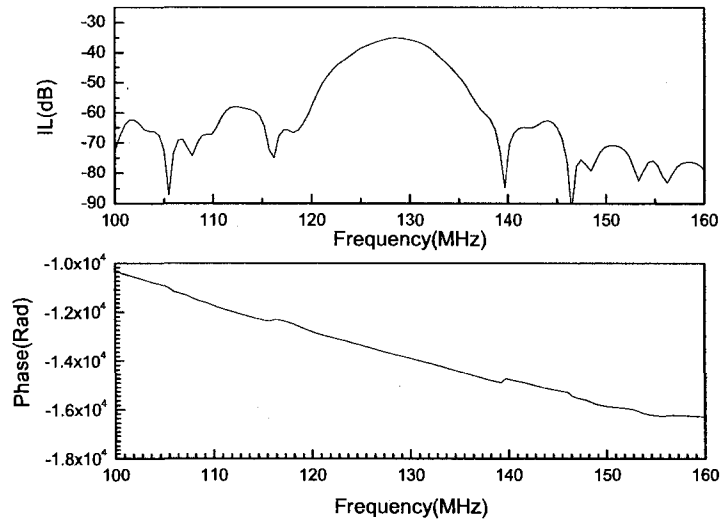


Figure 20: Frequency Response of SAW Sensor $F_c=130\text{MHz}$ with 0.3 H/Pd Concentration

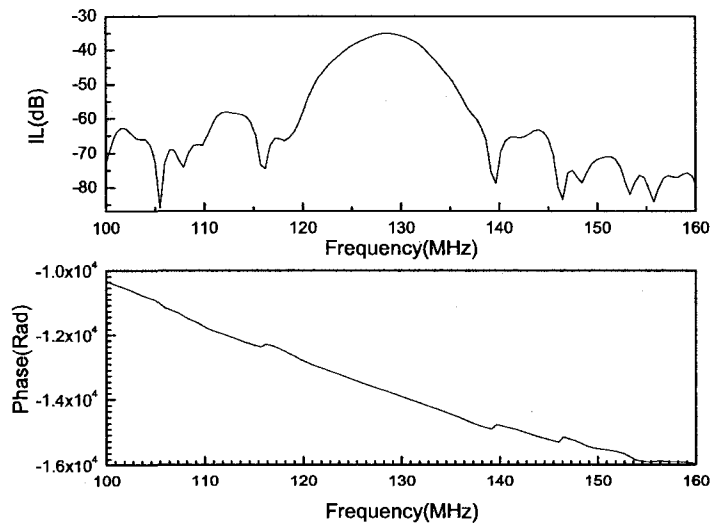


Figure 21: Frequency Response of SAW Sensor $F_c=130\text{MHz}$ with 0.4 H/Pd Concentration

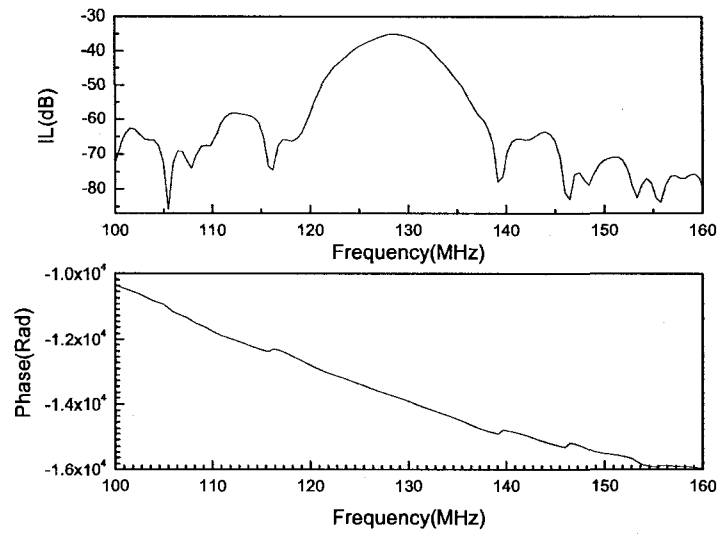


Figure 22: Frequency Response of SAW Sensor $F_c=130\text{MHz}$ with 0.5 H/Pd Concentration

Table 13: Simulation Results for Center Frequency and Insertion Loss for Different Hydrogen Concentration Cases using the Pd Coated YZ-LiNbO₃ SAW Device Operating at $F_c=130\text{MHz}$

$c(H/Pd)$	$f_c(\text{MHz})$	$IL(\text{dB})$
Bare Substrate	127.44	-32.813
Pure Pd	128.91	-35.764
0.1	128.91	-35.342
0.2	128.91	-35.14
0.3	128.42	-35.06
0.4	128.42	-35.028
0.5	128.42	-35.036

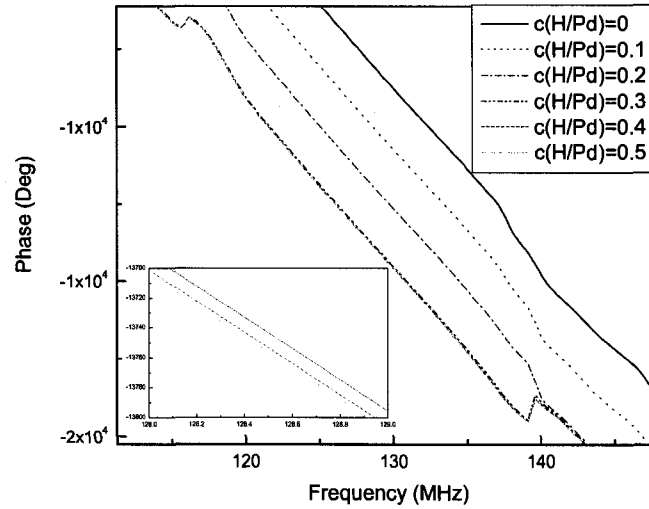


Figure 23: Phase Profiles at Different Hydrogen Concentrations Near the Center Frequency $F_c=130$ MHz. The Inset Illustrates the Phase Profiles for the 0.3-0.5a.f. Concentration Region

Table 14: Simulation for Phase Change Due to Various Hydrogen Concentrations in Pd Coated YZ-LiNbO₃ SAW Device Operating at $F_c=130$ MHz

$c(H/Pd)$	Phase $ \phi $ (Deg)	$ \Delta\phi $	$ \frac{\Delta\phi}{\phi} = \frac{\Delta v}{v} $
Pure Pd	12629	0	0.0000
0.1	13023	394	0.0312
0.2	13408	779	0.0617
0.3	13735	1106	0.0876
0.4	13745	1116	0.0884
0.5	13748	1119	0.0886

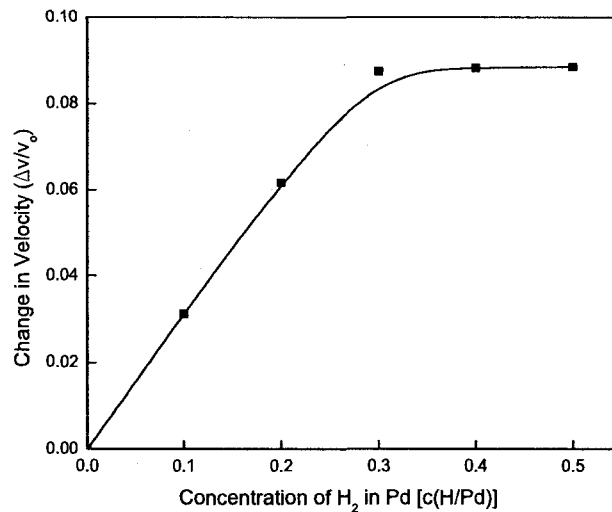


Figure 24: Change in Phase Velocity Due to Hydrogen Absorption

The change in frequency data in Table 13 illustrate that there has been a change in velocity. In the case of Pure Pd the center frequency of the film increased as compared to the bare substrate case, which indicates that the addition of the film helped to increase the wave velocity. However, the center frequency values up to a concentration of 0.2a.f. (atomic fraction) was 128.9MHz, however it decreased to 128.42MHz for the remaining concentration values.

Figure 23 shows the changes in the phase profiles for the various hydrogen concentration cases and the inset illustrates that the profiles in the 0.3-0.5a.f. concentration region continue to follow the same trend. The data in Table 14 shows that the absolute value of the phase increased as hydrogen concentration increased, which indicates a reduction in the wave velocity. The absolute values of the phase shift also increased with increasing hydrogen concentration. Figure 24 illustrates the change in wave velocity as a result of increasing hydrogen content. It is clearly seen that the change in velocity increases with increasing hydrogen content. This is due to the deterioration in the material properties of the Pd film. In the range 0.3-0.5a.f. the velocity change is much smaller.

Investigating the change in Pd film properties for the different concentrations was carried out. It was illustrated in (3-36) that the wave velocity is directly proportional to the stiffness constant and inversely proportional to density. The change in the stiffness constants of the Pd film with respect to the change in density was calculated for the different concentrations. Figure 25 and Figure 26 illustrate the change in stiffness constants c_{12} and c_{44} respectively with respect to change in density for the different hydrogen concentrations. It is clearly seen that in the 0.3-0.5a.f. range the slope is significantly reduced. These results validate the reduction in magnitude of the velocity change in the concentration region 0.3-0.5a.f. seen in Figure 24.

The insertion loss value increased from -32 to -35dB when the Pd film was added. This increase was expected and took place due to the mass loading effect of the film. However, at increasing hydrogen concentrations the insertion loss values decreased due to the softening of the Pd film. Figure 27 illustrates the change in insertion loss for the different hydrogen concentrations. The change in insertion loss values in the concentration region of 0.3-0.5a.f. is reduced due to the reduction in magnitude of the change in film properties.

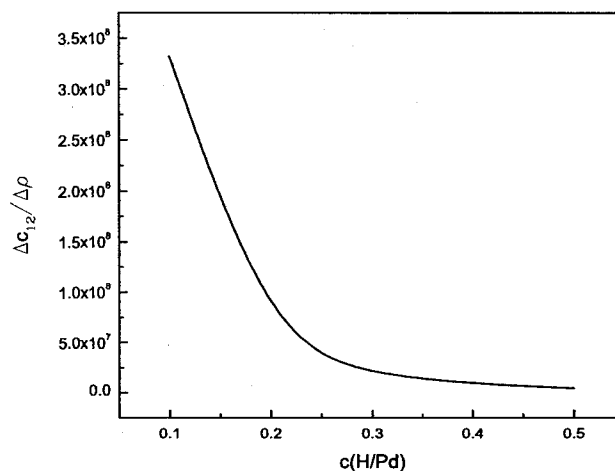


Figure 25: The Change in First Lamé Constant with Respect to Change in Density of the Palladium Film at Different Hydrogen Concentrations

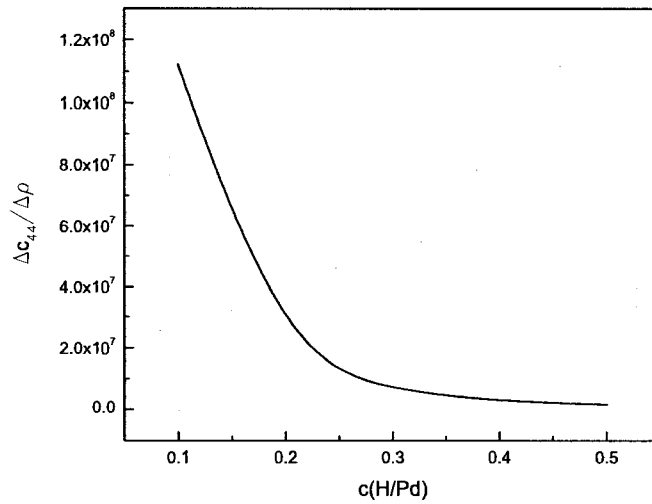


Figure 26: The Change in Second Lamé Constant with Respect to Change in Density of the Palladium Film at Different Hydrogen Concentrations

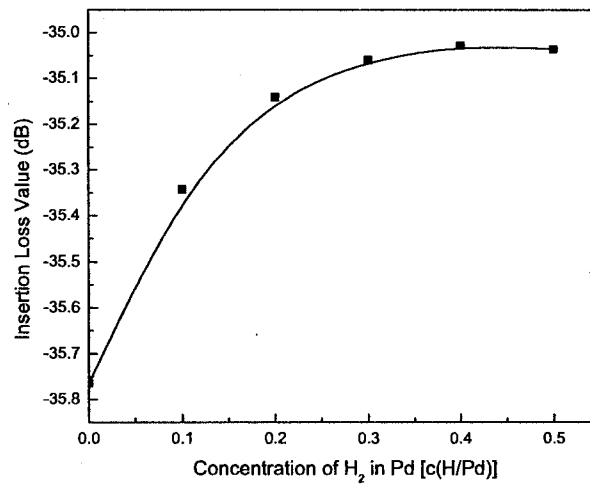


Figure 27: Insertion loss values at Different Hydrogen Concentrations

Chapter 5

5 A Reduced 3D Model for Surface Acoustic Wave Sensors

5.1 Introduction

The goal in sensing applications is to develop a fully integrated system on one chip referred to as a Monolithic Chip [52]. The chip combines the sensor and other essential electronic circuitry such as power supply, signal conditioning circuit elements, antenna in case of wireless applications, etc. The platform for Monolithic chips is Silicon. The advantages of integrating all components on one chip is the reduction in size, low cost, mass production, low power consumption etc.

Developing SAW sensors on Silicon wafers requires compatibility between the SAW sensor fabrication process with that of planar integrated circuits. Bulk piezoelectric materials such as Lithium Niobate, Quartz, Lithium Tantalate, etc are incompatible with planar integrated circuit technology. Consequently layered SAW sensors have been adopted, which consist of a Silicon substrate and a thin piezoelectric film. The piezoelectric thin film is deposited on top of the Silicon using Thin Film Deposition Technology, which is compatible with planar integrated circuit technology. There are two piezoelectric materials widely used for such applications these are Zinc Oxide (ZnO) and Aluminum Nitride (AlN) [53].

Both materials exhibit desirable properties. Zinc Oxide has a high electromechanical coupling coefficient and excellent bonding on Silicon. Aluminum Nitride (AlN) on the other hand is widely used especially in high frequency applications due to its very high acoustic velocity 5,607m/s [54]. SAW devices based on AlN operating at frequencies in the range of 5-6GHz have been developed [55]. The high velocity eliminates the need for high resolution photolithographic processes.

The next step in this study was to modify the model to the Silicon-Piezoelectric Thin Film layout. A 3D model was developed for the AlN/Si configuration. However, a mesh convergence could not have been reached and the number of elements was increasing the size of the model significantly.

The assumed solutions of the wave equations for a wave propagating along the x -direction with polarization in the y -direction are [29]:

$$\begin{aligned} u_i &= \alpha_i \exp(ikby) \exp(ik(x-vt)) \\ \phi &= \alpha_i \exp(ikby) \exp(ik(x-vt)) \end{aligned} \quad (5-1)$$

where ' b ' denotes the variation with depth and ' α ' gives the amplitude of the waves, ' k ' is the wave number and ' v ' is the Phase velocity. It is obvious that the solutions of the displacement and voltage depend on the x and y directions only. No variation takes place along the z -direction. This is the plane wave solution. This fact can be used to reduce the size of the sensor in the z -direction since it does not matter how thick the model is. The model can therefore become a *Reduced* 3D model. This approach was adopted using ANSYS® 11.0.

5.2 Reduced 3D AlN/Si(111) Model

The model consists of a Silicon substrate with the crystal axis oriented such that the [111] direction is perpendicular to the top surface. On top of the Silicon substrate a thin Aluminum Nitride film is placed. The electrodes are placed on the free surface of the Aluminum Nitride film. A schematic of the sensor is illustrated in Figure 28.

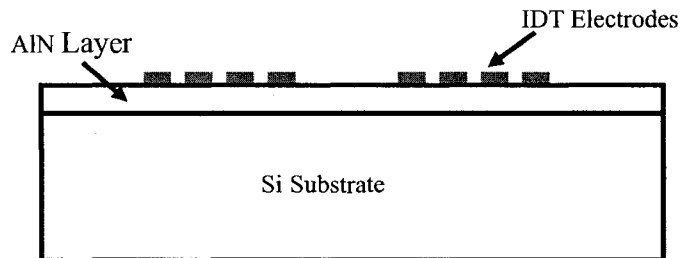


Figure 28: Schematic of AlN/Si(111) SAW Device

The elastic constants for Silicon in the [100] direction are obtained and were rotated accordingly to generate the properties in the [111] direction. The material properties of Si(100) are obtained from Madou [45]. Silicon has a Cubic crystal structure and hence has three independent elastic constants; $c_{11}=166$, $c_{12}=64$, $c_{44}=80$ GPa. The Density $\rho=2,320\text{Kg/m}^3$.

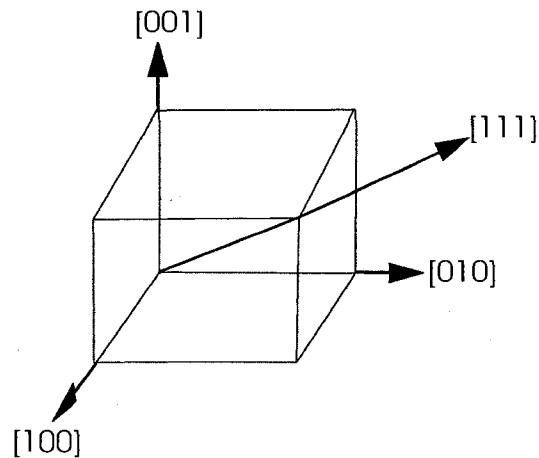


Figure 29: Silicon Crystal with Crystallographic Directions

The [111] direction is at an angle of 54.74 from the [001] axis. The crystal axis had to be rotated about the origin such that the [111] axis is vertically upwards. The procedure for this rotation is straight forward. Three rotation matrices had to be defined. A rotation matrix for rotating the crystal 45 about the [001]. A second rotation matrix that rotates the crystal -54.74 about the [010] axis in the new position. A final rotation matrix that rotates the crystal -45 about the final position of the [001] axis.

The material properties for Aluminum Nitride are listed in Table 15. Aluminum Nitride has a density $\rho=3,260\text{Kg/m}^3$. All properties have been obtained from [56].

Table 15: Material Properties of Aluminum Nitride

Elastic Matrix In Stiffness Form ($\times 10^{11}$ Pa)		Piezoelectric Matrix at Constant Strain (C/m^2)		Permittivity Matrix at Constant Strain ($\times 10^{-11}$ F/m)	
C_{11}	3.45	e_{15}	-0.48	ϵ_{11}	8
C_{12}	1.25	e_{31}	-0.58	ϵ_{33}	9.5
C_{13}	1.2	e_{33}	1.55		
C_{33}	3.95				
C_{44}	1.18				
C_{66}	$\frac{C_{11} - C_{12}}{2} = 1.1$				

The FE model of the SAW sensor is illustrated in Figure 30. The electrodes were modeled as a set of nodes coupled with a voltage degree of freedom. In this model the electrodes have the same length in the z-direction as the device thickness. It is as if a thin strip at the center of the full 3D model is being analyzed. Figure 31 illustrates the electrodes at the surface of the sensor.

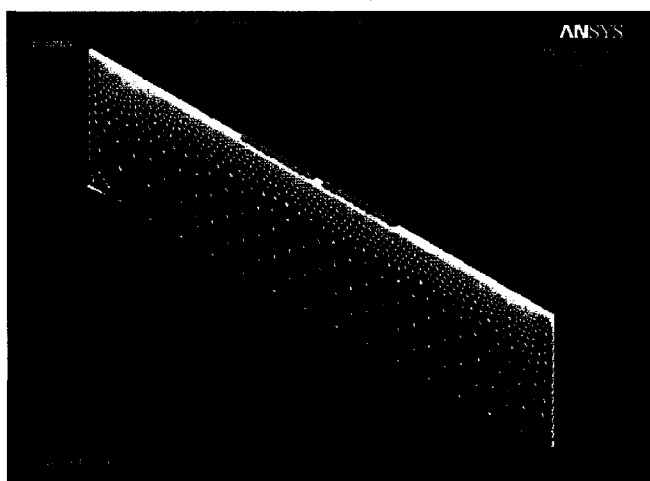


Figure 30: Finite Element Model of AlN/Si(111) Reduced 3D Model

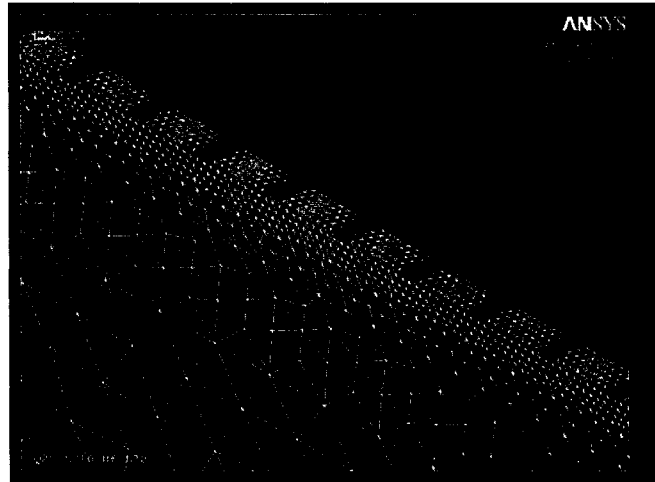


Figure 31: Electrodes in the Reduced 3D AlN/Si(111) Model

5.2.1 Boundary Conditions

The boundary conditions adopted in this model are slightly different to the previously developed XY-LiNbO₃ ZnO model although both are layered devices. In this model the region S refers to the region outside the IDT's on the AlN surface. The boundary conditions are listed in Table 16 with comparison to previous models.

Table 16: Boundary Conditions for Reduced 3D AlN/Si(111) Model

Boundary Conditions		XY-LiNbO ₃ ZnO Model	YZ-LiNbO ₃ Model	Reduced 3D AlN-Si(111) Model
Clamped Condition on A_1	$(u_x, u_y, u_z, \phi = 0)$	✓	✓	✓
Dirichlet Conditions	$\phi _{R1} = 0$ $\phi _{R2} = V(t)$ $\phi _{R3} = O(t)$	✓	✓	✓
Continuity of the Displacement field at Interface $I^{(a)}$	U_i for $i = x, y, z$	✓	✓	✓
Continuity of the Voltage at Interface I	ϕ	✓	✗	✗
Traction Free Boundary at S	$T_{iz} = 0$; for $i = x, y, z$	✓	✓	✓
Extension of Boundaries	B_1, B_2, W_1 & W_2	✓	✓	✓

5.2.2 Simulation Parameters

5.2.2.1 Element Type

The Silicon substrate was meshed with the 3D Solid98 10 node tetrahedral Coupled Field element. There are up to six degrees of Freedom per node. The Key-options of the element were set to allow only structural degrees of freedom per node; U_x , U_y and U_z . The Aluminum Nitride film was meshed with Solid226 3D Coupled Field Solid element. There are three structural degrees of freedom per node; U_x , U_y and U_z and one electrical degree of freedom; Voltage (V).

5.2.2.2 Mesh Sensitivity Analysis

A mesh sensitivity analysis was initially performed. It was desired to determine the number of elements per wavelength required to fully capture the wave. An impulse signal is applied to the electrodes to determine the impulse response, the signal is defined in (4-2). The frequency response was determined from the Fourier Transform of the Impulse response. The parameters of the sensor used in the mesh sensitivity analysis are listed in Table 17.

Table 17: Parameters of the AlN/Si(111) Model Used in Mesh Sensitivity Analysis

Parameters	Parameter Value
<i>Dimensions of the Si(111) Substrate</i>	2000x500x11 μ m
<i>Dimensions of the AlN Substrate</i>	2000x6x11 μ m
<i>Number of Electrode Pairs</i>	10
<i>Wavelength</i>	30 μ m
<i>Electrode width and Spacing</i>	$\lambda/4$
<i>Separation Distance</i>	2λ
<i>Thickness of AlN Film</i>	6 μ m

The criterion for convergence was the center frequency. The different element sizes and the corresponding center frequencies are listed in Table 18. Figure 32 illustrates the convergence of mesh sensitivity analysis at element size of 2 μ m. This element size was chosen for the rest of this study.

Table 18: Parameters for Mesh Sensitivity Analysis for AlN/Si(111) SAW Model

<i>Element Size</i>	<i>Number of Elements/Wavelength ($\lambda=30\mu\text{m}$)</i>	<i>Center Frequency</i>
2	15	147.95
3	10	148.44
4	7.5	148.93
8	3.75	150.39
12	2.5	154.79
16	1.875	161.13
20	1.5	171.87

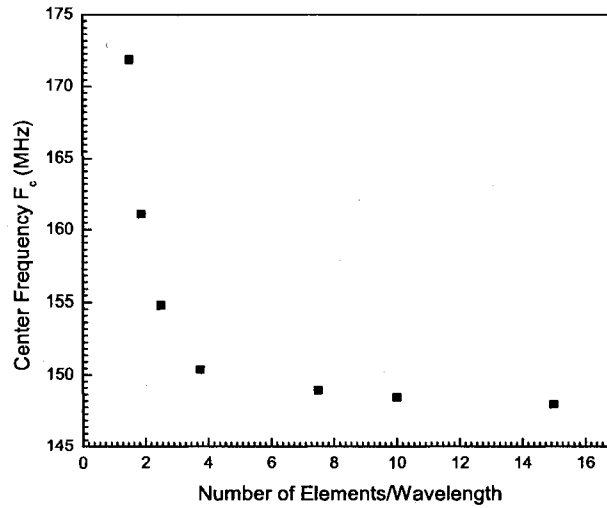


Figure 32: Mesh Sensitivity Analysis for 11 μm Thick AlN/Si(111) SAW Model

Initially a check whether the effect of thickness would influence the sensor response was performed. The sensor was set to an initial thickness of $T_0=11\mu\text{m}$. this was the minimum thickness that could be selected without violating any restrictions on element shapes. The thickness was increased and in each case the center frequency and the IL of the sensor were recorded.

Figure 33 and Figure 34 illustrate the frequency response and the insertion loss values for the AlN/Si(111) model respectively for different thicknesses. The variation in the frequency is between 146-149MHz. The variation in the Insertion

Loss is between -53 and -57dB. As expected increasing the thickness has negligible effect on sensor response. The thickness will be kept at $11\mu\text{m}$ for the rest of this study.

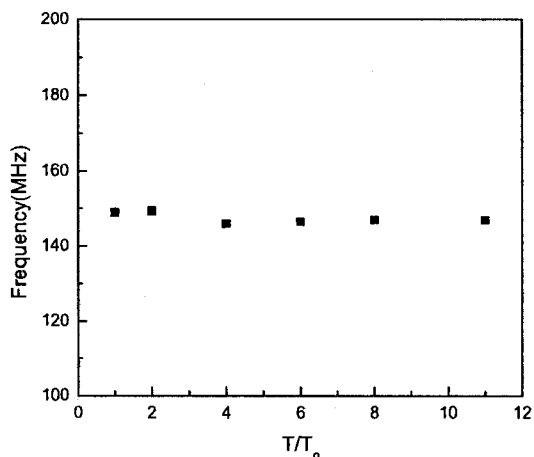


Figure 33: The Effect of Model Thickness on Center Frequency of the AlN/Si(111) Model

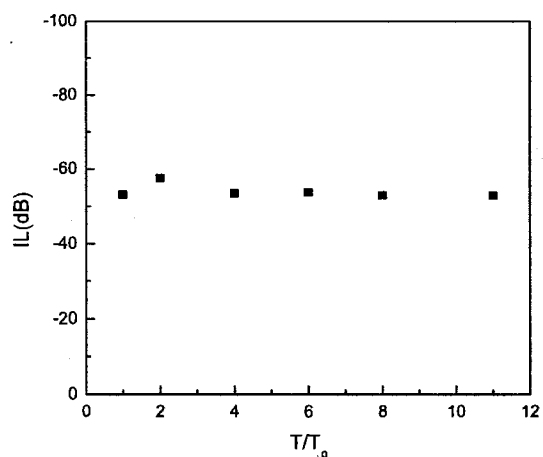


Figure 34: The Effect of Model Thickness on Insertion Loss of the AlN/Si(111) Model

Another check was made where the boundaries were gradually extended to determine the length that would cancel their effect on the sensor response. Different lengths were selected. L_0 is the distance between the boundary and the input/output

IDT in the first case where the substrate length is $1000\mu\text{m}$. As the substrate length increased the distance to the boundary increased and was expressed as a ratio L/L_0 . The center frequency and IL values were determined for each case. The results are plotted in Figure 35 and Figure 36. The center frequency and the insertion loss indicate that the influence of the boundary on the sensor response was not significant. The variation in the frequency is between 146-149MHz. The variation in the Insertion Loss is between -52 and -53dB. The minimal effect on response could be due to the high magnitude of the signal that could not have been significantly distorted by the reflections at the boundaries.

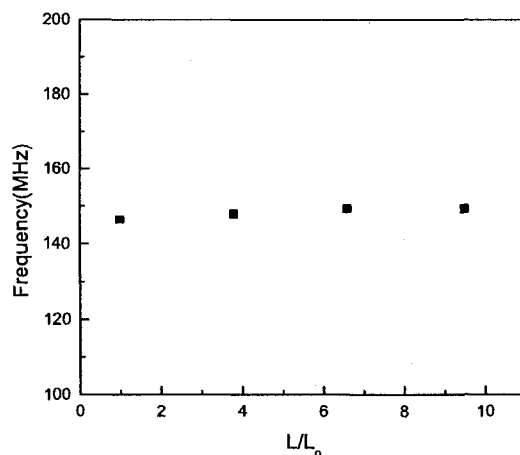


Figure 35: The Effect of Substrate Length on Center Frequency of AlN/Si(111) Model

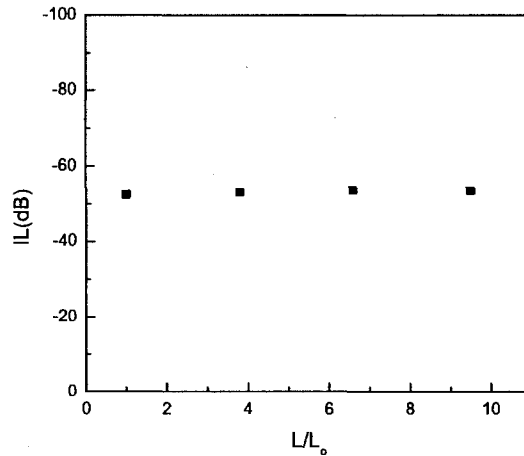


Figure 36: The Effect of Substrate Length on Insertion Loss of AlN/Si(111) Model

5.3 Results

SAW velocity in AlN is higher than Silicon; 5607 and 4550m/s respectively [54]. Adding a thin piezoelectric layer on the Silicon substrate increases the phase velocity of the wave on the surface. As the thickness of the piezoelectric film increases the wave becomes more confined in the piezoelectric film and hence its velocity increases proportionally. As the film thickness increases the velocity increases to a limit when it is completely confined in the AlN layer and hence its velocity approaches the AlN phase velocity value. Velocity dispersion data relates the SAW phase velocity in the AlN/Si(111) configuration to the normalized parameter h/λ . The thickness of the AlN film is denoted by ' h ' and ' λ ' is the wavelength. Theoretical dispersion data [54] were used for comparison with the simulation results. The thickness of the AlN film was set to a fixed value and the wavelength was changed to test different cases. A Transient analysis was carried out where an impulse signal ((4-2)) was applied to the electrodes to determine the impulse response. The center frequency was determined from the Fourier Transform of the Impulse response and was used for comparison with the theoretical data. The simulation time was varied with the configuration and is shown for each case in the Impulse response plots in Figure 37 to Figure 41.

The velocity values from the dispersion data (V_{th}) were multiplied with the various wavelength values to determine the corresponding theoretical frequencies (F_{th}). The theoretical frequency values were compared with the simulation frequencies (F_{sim}). The data used in this analysis is listed in Table 19.

Table 19: Theoretical Velocity Data for AlN/Si(111) Reduced 3D Model [54]

h/λ	$h(\mu m)$	$\text{Lambda}(\lambda)$ (μm)	$V_{Th}(m/s)$	$F_{Th}(MHz)$
0.1	6	60.00	4570	76.17
0.11	6	54.55	4575	83.88
0.14	6	42.86	4586.67	107.02
0.17	6	35.29	4608.3	130.57
0.2	6	30.00	4633.33	154.44

The parameters of the sensor for each case in Table 19 are the same except for the wavelength. These parameters are listed in Table 20.

Table 20: Parameters of the AlN/Si(111) Models used in Comparison with Dispersion Curve Data

Parameters	Value
<i>Dimensions of the Si(111) Substrate</i>	3000x500x11 μm
<i>Dimensions of the AlN Substrate</i>	3000x6x11 μm
<i>Number of Electrode Pairs</i>	10
<i>Electrode width and Spacing</i>	$\lambda/4$
<i>Separation Distance</i>	2λ
<i>Thickness of AlN Film</i>	6 μm

Figure 37 to Figure 41 illustrate the time and frequency domain responses for each case in Table 19. Table 21 summarizes the results for the different cases.

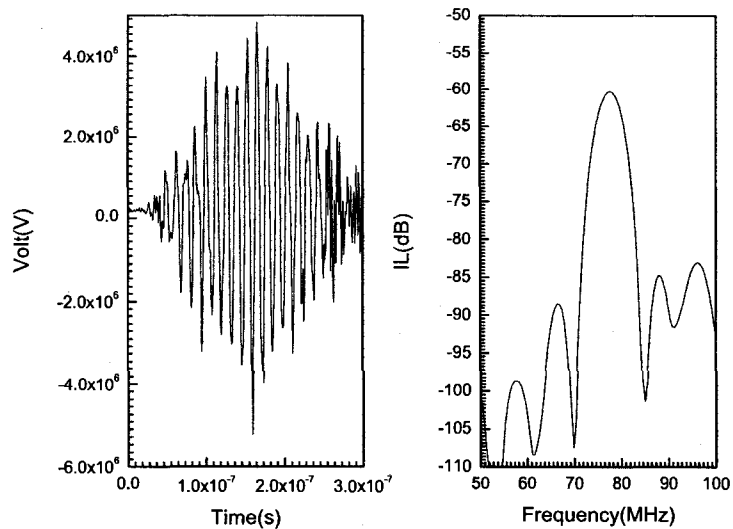


Figure 37: Time and Frequency Domain Responses for $h/\lambda=0.1$ AlN/Si(111) Configuration

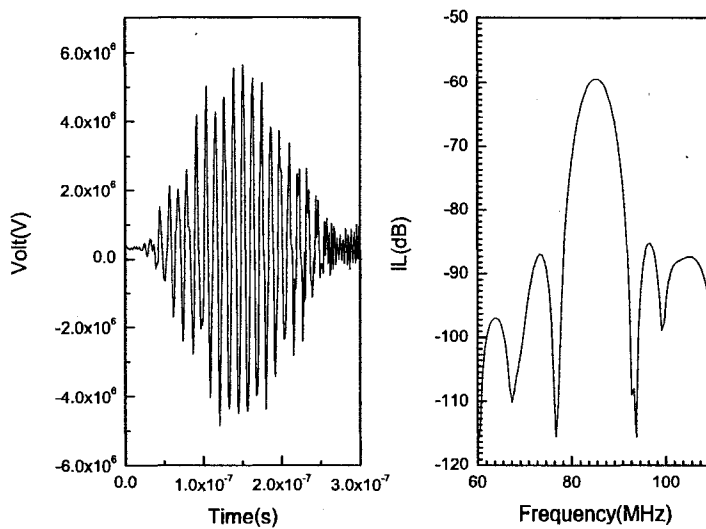


Figure 38: Time and Frequency Domain Responses for $h/\lambda=0.11$ AlN/Si(111) Configuration

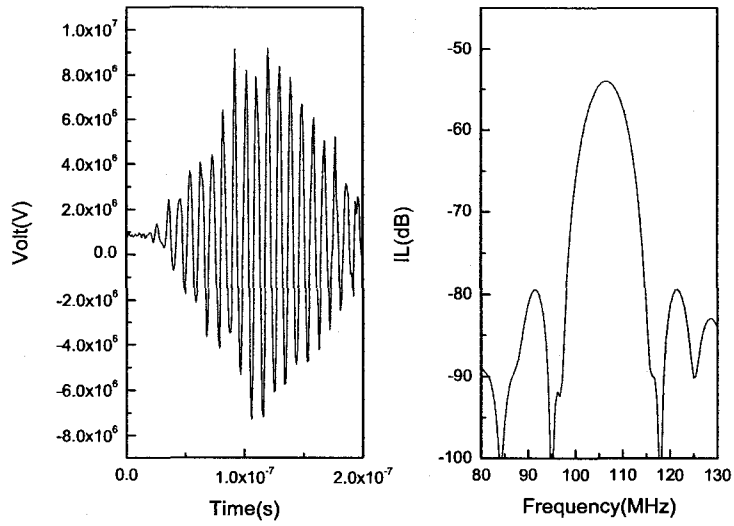


Figure 39: Time and Frequency Domain Responses for $h/\lambda=0.14$ AlN/Si(111) Configuration

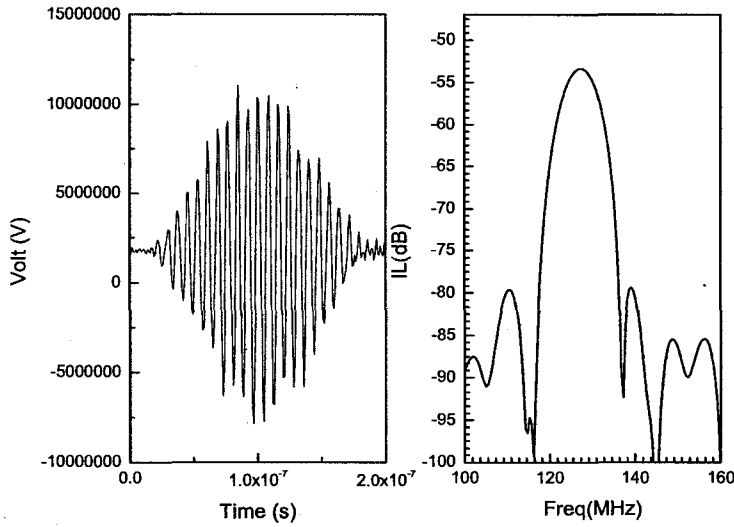


Figure 40: Time and Frequency Domain Responses for $h/\lambda=0.17$ AlN/Si(111) Configuration

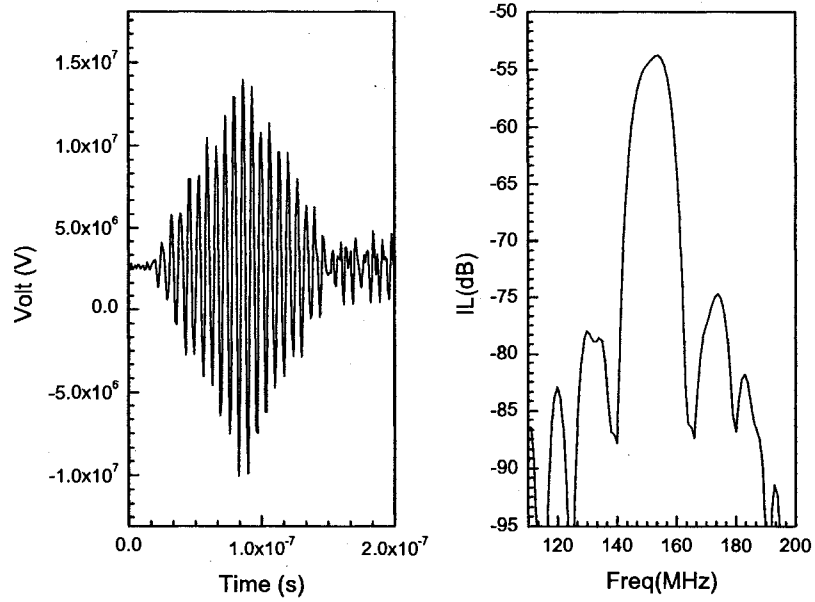


Figure 41: Time and Frequency Domain Responses for $h/\lambda=0.2$ AlN/Si(111) Configuration

Table 21: Center Frequency Data for AlN/Si(111) Reduced 3D Model

h/λ	$h(\mu\text{m})$	$\text{Lambda}(\lambda)$ (μm)	$V_{Th}(m/s)$	$F_{Th}(MHz)$	$F_{Sim}(MHz)$	%ERROR
0.1	6	60	4570	76.2	77.637	1.93
0.11	6	54.55	4575	83.875	85.45	1.88
0.14	6	42.86	4586.67	107.02	106.45	0.53
0.17	6	35.29	4608.3	130.56	127.44	2.4
0.2	6	30	4633.33	154.44	147.95	4.2

The frequency values from the simulation were plotted against the theoretical values and are illustrated in Figure 42.

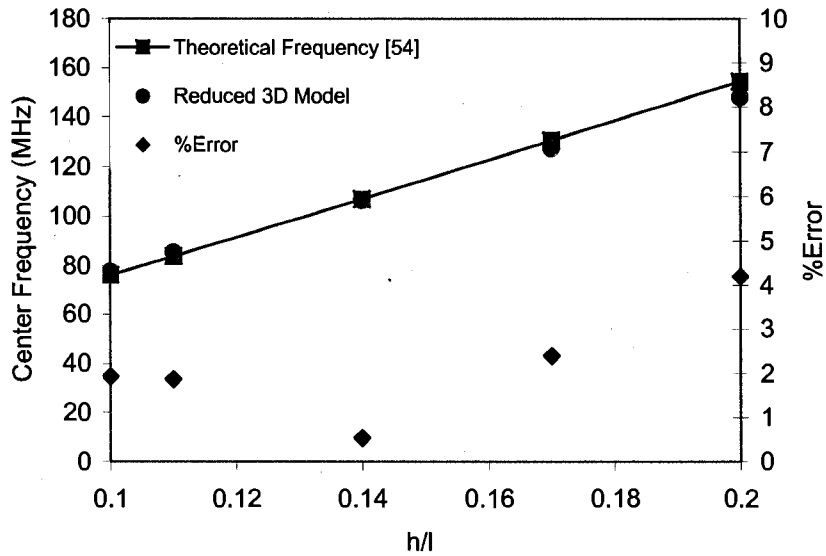


Figure 42: Comparison between Simulation and Theoretical Frequency values for AlN/Si(111)

A two dimensional model for each of the cases in Table 19 was built and compared with the theoretical and Reduced 3D model. The models were compared in terms of the center frequency and the insertion loss values. The center frequency data are listed in Table 22 and plotted in Figure 43. The insertion loss data are listed in Table (23) and plotted in Figure 44.

Table 22: Comparison of Center Frequency Data of AlN/Si(111) Reduced 3D Model and 2D Model with Theoretical Frequency Data

h/λ	Theoretical Frequency F_{th} (MHz)	Reduced 3D Model F_{sim} (MHz)	2D Model F_{sim} (MHz)
0.1	76.16667	77.637	73.73
0.11	83.875	85.45	80.566
0.14	107.0223	106.45	101.56
0.17	130.5685	127.44	122.56
0.2	154.4443	147.95	142.09

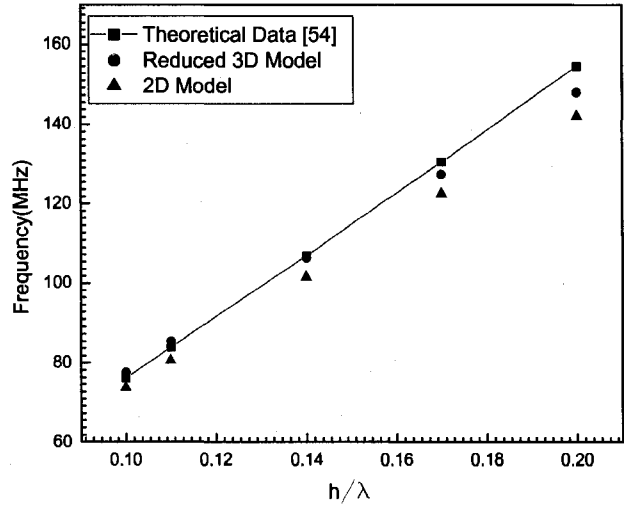


Figure 43: Comparison of Center Frequency between Reduced 3D Model and 2D Model for AlN/Si(111)

Table 23: Comparison of Insertion Loss Data of AlN/Si(111) Reduced 3D Model and 2D Model

h/λ	Reduced 3D Model IL(dB)	2D Model IL(dB)
0.1	-60.245	-75.444
0.11	-59.363	-74.358
0.14	-53.98	-69.315
0.17	-53.364	-68.225
0.2	-53.178	-67.212

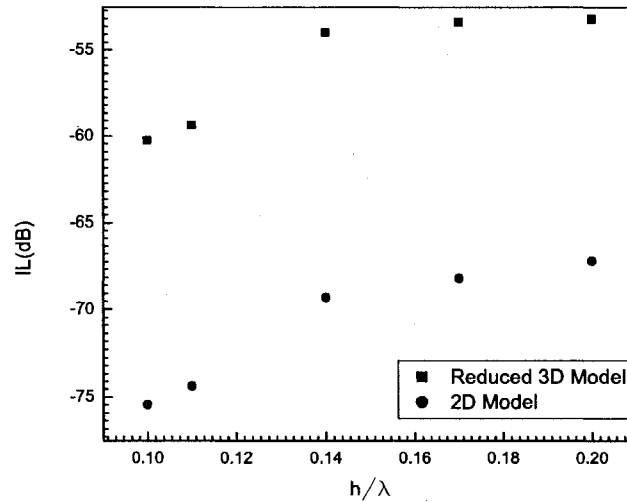


Figure 44: Comparison of IL Values for Reduced 3D Model and 2D Model for AlN/Si(111)

The results in Figure 42 illustrate that the center frequency from the reduced 3D model agrees very well with the theoretical frequency data. The maximum error was 4% in the 154MHz case. In addition, the reduced 3D model showed that it could yield better results than the 2D model. Results in Figure 43 and Figure 44 illustrate that the difference between the 2D model and the reduced 3D model is significant and should not be neglected.

The results using the reduced 3D model are very promising especially that this model requires around 70,000 elements as opposed to 200,000 in the 3D YZ Lithium Niobate model. This difference in element number is appreciable and hence reduces the computational time significantly. The reduced 3D model therefore helps to solve one of the major problems in modeling SAW devices. The increased size of the model and hence the prolonged computational time have been obstacles in the face of other researchers who tried to model SAW devices using Finite Element. This often pushed them to adopt other techniques for reducing the size of the model, which affected the accuracy of the results. Atashbar [23] had to reduce the depth of the model significantly and hence the top and bottom surfaces were very close. In addition, the boundaries were not extended to reduce reflection. The results indicate

that there was significant distortion to the response especially that the chosen number of electrodes were very few. Ippolito *et al* [57] on the other hand, although extended the boundaries to eliminate reflections claims that inaccuracies in the finite element model in comparison with the experimental results are attributed to the insufficient node density.

The reduced 3D model avoids all these problems and does not require extensive memory capabilities. In addition, the simulation run time is significantly reduced. This gives the researcher flexibility in other issues in the model such as reaching higher frequencies, adding thin film in the propagation path or adding more material layers to the sensor.

Chapter 6

6 Conclusions and Future Work

6.1 Summary and Conclusions

Acoustic Wave devices range in their configurations and designs. The most commonly used acoustic wave devices are the Quartz Crystal Microbalance (QCM), Shear Horizontal Acoustic Plate Mode Devices (SH-APM), Flexural Plate Wave Devices (FPW) and the Surface Acoustic Wave Devices (SAW). The operating principles of all these acoustic devices except the SAW device are presented in Chapter 2. The operating principle of the SAW device is discussed in detail in Chapter 3. Acoustic Wave devices play an important role in many sensing applications that range from strain sensing, pressure sensing, gas sensing, liquid sensing, detection of ice formation and viscosity sensing as discussed in Chapter 1.

The ability to model a SAW device for a given application could save both time and money in experiments. There are various modeling techniques that can be used in the design process such as the Coupling of Modes (COM) technique, Equivalent Circuit Model, Finite Difference (FD) and Finite Elements (FE). Examples of the application of these modeling techniques to SAW devices are mentioned in Chapter 2.

Chapter 3 introduced the Stress, Strain and Particle Displacement Fields. The equation of motion is then derived for a vibrating particle. These concepts are utilized in deriving of the wave equation in a non-piezoelectric solid. The goal is to derive the wave equation in a piezoelectric solid, therefore the piezoelectric constitutive relations are introduced and the wave equations in a piezoelectric solid are derived in a similar fashion to the non-piezoelectric case. The finite element formulation is then briefly introduced to show how these equations are solved. In the same chapter the principles of operation of the interdigital Transducer (IDT) is explained. Finally,

different wave perturbation mechanisms are introduced. The relation between the change properties of the wave as a result of interaction with the measurand and the energy and power densities of the wave is explained.

Chapter 4 introduced the first model that was built for the XY-LiNbO₃ ZnO configuration. This model was built to verify the results with experimental and simulation results in the literature. The model was then changed to a bare YZ-LiNbO₃ substrate to test for different cases of Hydrogen absorption. A thin Palladium (Pd) film was added along the propagation direction, which is the chemically selective film. Five cases were tested for hydrogen absorption in the concentration range 0.1-0.5a.f. For each case the material properties of Palladium were changed accordingly. A transient analysis was carried out. The frequency response of the sensor was obtained using a Fourier Transform code developed using MatLAB®. The phase profiles were compared for the different cases and the change in phase with respect to the pure Pd case was calculated. The normalized change in phase was used to determine the velocity change for each case. The results indicated an increasing trend for the changes in velocity. This result was expected. As the Pd film absorbs hydrogen the film softens and therefore the velocity of the wave in the film is reduced. In the concentration range 0.3-0.5a.f. the change in material properties was small and therefore the change in wave velocity decreased.

Chapter 5 discussed the issue of developing SAW sensors using Silicon substrates to have a monolithic chip that includes the sensor with all the electronic circuitry. While attempting to build the 3D model of a SAW sensor using a silicon substrate, there were problems of model size. Upon studying the assumed solutions of the wave equation it was discovered that the solutions do not vary with the lateral direction. This fact was used to reduce the size of the model in the lateral direction, which helped to reduce the model size significantly. The reduced 3D model consisted of an AlN thin film on a Silicon substrate. Theoretical velocity data were obtained for the AlN-Si configuration adopted. The data illustrate the changes in velocity values as the normalized parameter (h/λ) changes, where h is the thickness of the AlN film and λ is the wavelength. The thickness of the film was maintained at a constant value and the

wavelengths were changed to test for the different cases. The frequency response of the model was obtained using Fourier Transform of the impulse response. The resulting center frequency was recorded for each case. The theoretical velocity values were multiplied with the wavelength to generate the theoretical frequencies. The simulation and theoretical frequencies were compared and the results showed good agreement. Finally the response of the reduced 3D model was compared with that of 2D models, which is the configuration widely adopted in the literature. Results from both models were compared using theoretical data. The reduced 3D model yielded more accurate results.

6.2 Future Work

There are several issues that need further work both in the case of hydrogen detection and the reduced 3D model.

For the case of hydrogen detection:

- Different center frequencies should be used to study the sensitivity of the sensor.
- The influence of other parameters on the response should be tested such as the number of electrodes, the thickness of the Pd film, the propagation area, etc. This would lead to an optimum set of parameters for the case of hydrogen detection.
- The results of the velocity change are conclusive but further verification with experimental data would enrich the value of the model.

For Reduced 3D Model:

- The model should be applied to a case of sensing application. This would provide means of assessing the response and will give an indication of its suitability for sensing applications.

- Fabricating an AlN-Si SAW device and comparing its response with the model. Experimental data would enhance the validity of the model significantly.
- The model used for YZ-LiNbO₃ model should be changed to the reduced 3D configuration. The different cases of hydrogen absorption could be re-tested and a comparison with the full 3D model would be interesting to study.

References

1. Rayleigh, L., *On Waves Propagated Along the Plane Surface of an Elastic Solid*. Proceedings of the Londong Mathematical Society, 1885. **1**(1-17): p. 4-11.
2. Morgan, D.P. *History of SAW Devices*. in *IEEE International Frequency Control Symposium*. 1998. Pasadena, CA, USA.
3. White, R. M. and Voltmer, F. W., *Direct Piezoelectric Coupling to Surface Elastic Waves*. Applied Physics Letters, 1965. **7**(12): p. 314-316.
4. Ballantine, D. S., White, R. M; Martin, S. J; Ricco, A. J; Frye, G. C., Zellers, E. T. and Wohltjen, H., *Acoustic Wave Sensors; Theory, Design and Physico-Chemical Applications*. 1997: Academic Press.
5. Kondoh, J., Matsui, Y. and Shiokawa, S., *New Biosensor Using Shear Horizontal Surface Acoustic Wave Device*. Japanese Journal of Applied Physics, 1993. **32**(5B): p. 2376-2379.
6. Martin, F., Newton, M., McHale, G., Melzak, K. and Gizeli, E., *Pulse Mode Shear Horizontal Surface Acoustic Wave (SH-SAW) System for Liquid Based Sensing Applications*. Biosensors and Bioelectronics, 2004. **19**: p. 627-632.
7. Josse, F., Bender, F. and Cernosek, R., *Guided Shear Horizontal Surface Acoustic Wave Sensors for Chemical and Biochemical Detection in Liquids*. Analytical Chemistry, 2001. **73**: p. 5937-5944.
8. Lee, Y., Yoon, D. and Kim, T., *Improvement of the Mass Sensitivity in Flexural Plate Wave Biosensor Based on PZT Thin Film*. Integrated Ferroelectrics, 2005. **69**(1): p. 391-400.
9. Black, J., Chen, B., Quinn, R., Madou, M. and White, R. *Comparison of the performance of flexural plate wave and surface acoustic wave devices as the detector in a gas chromatograph*. in *Proceedings of the IEEE Ultrasonics Symposium*. 2000.
10. Schofield, A., Rudd, T., Martin, D., Fernig, D. and Edwards, C., *Real Time Monitoring of the Development of the Stability of Biofilms of Streptococcus Mutans using the Quartz Crystal Microbalamance with Dissipation Monitoring*. Biosensors and Bioelectronics, 2007. **23**: p. 407-413.
11. Wang, S.T., Chung, M., Shen, C. and Huang, A.C.S. *Determination of Equivalent Circuit Model Parameters from Coupling-of-Modes Theory*. in *IEEE Ultrasonics Symposium. Proceedings*. 2002.

12. Suzuki, Y., Takeuchi, M., Nakamura, K. and Hirota, K., *Coupled Mode Theory of SAW Periodic Structures*. Electronics and Communications in Japan, 1993. **76**(3): p. 87-95.
13. Ntagwirumugara, E., Gryba, T., and Lefebvre, J. E. *Design of Al/ZnO/Si one-port SAW resonator filter*. in *Proceedings - 8th International Symposium on Signal Processing and its Applications*. 2005.
14. Lee, K., Wang, W., Kim., G. and Yang, S., *Surface Acoustic Wave Based Pressure Sensor with Ground Shielding over Cavity on 41 YX LiNbO₃*. Japanese Journal of Applied Physics, 2006. **45**(7): p. 5974-5980.
15. Campbell, C., *Surface Acoustic Wave Devices and Their Signal Processing Applications*. 1989: Academic Press Inc.
16. Liu, Yi. and Cui, T., *Power Consumption Analysis of Surface Acoustic Wave Sensor Systems using ANSYS and PSPICE*. Microsystems Technologies, 2007. **13**(1): p. 97-101.
17. Inagawa, K. and Koshiha, M., *Equivalent Networks for SAW Interdigital Transducers*. IEEE Transactions on Ultrasonics, Ferroelectrics and Frequency Control, 1994. **41**(3): p. 402-411.
18. Wong, K. Y. and Tam, W. Y., *Analysis of the frequency response of SAW filters using finite-difference time-domain method*. IEEE Transactions on Microwave Theory and Techniques, 2005. **53**(11): p. 3364-3370.
19. Jatkar, D. and Beker, B., *Effects of Package Parasitics on the Performance of SAW Filters*. IEEE Transactions on Ultrasonics, Ferroelectrics, and Frequency Control, 1996. **43**(6): p. 1187-1194.
20. Lerch, R., *Simulation of Piezoelectric Devices by Two- and Three-Dimensional Finite Elements*. IEEE Transactions on Ultrasonics, Ferroelectrics, and Frequency Control, 1990. **37**(2): p. 233-247.
21. Ippolito, S.J., Kalantar-Zadeh, K., Powell, D. A. and Wlodarski, W. *A Finite Element Approach for 3-Dimensional Simulation of Layered Acoustic Wave Transducers*. in *Conference on Optoelectronic and Microelectronic Materials and Devices*. 2002. Sydney, NSW, Australia.
22. Ippolito, S.J., Kalantar-Zadeh, K., Wlodarski, W. and Powell, D. A. *Finite-Element Analysis for Simulation of Layered SAW Devices with XY LiNbO₃ Substrate*. in *Smart Structures, Devices, and Systems*. 2002.
23. Atashbar, M.Z., Bazuin, B. J., Simpeh, B. M., Krishnamurthy, S., *3D FE Simulation of H₂ SAW Gas Sensor*. Sensors and Actuators B, 2005. **111-112**: p. 213-218.

24. Botkin, N., Schlensog, M., Tewes, M. and Turova, V. *A Mathematical Model of a Biosensor*. in *International Conference on Modeling and Simulation of Microsystems*. 2001.
25. Xu, G., *Direct finite-element analysis of the frequency response of a Y-Z lithium niobate SAW filter*. *Smart Materials and Structures*, 2000. **9**(6): p. 973-980.
26. Xu, G. and Jiang, Q., *A finite element analysis of second order effects on the frequency response of a SAW device*. *Journal of Intelligent Material Systems and Structures*, 2001. **12**(2): p. 69-77.
27. Auld, B.A., *Acoustic Fields and Waves in Solids*. Vol. 1. 1973: John Wiley & Sons.
28. Auld, B.A., *Acoustic Fields and Waves in Solids*. Vol. 2. 1973: John Wiley & Sons.
29. Mason, W.P., ed. *Physical Acoustics Principles and Methods*. Vol. 9. 1972, Academic Press: New York.
30. ANSYS® Multiphysics, R., Help System, Theory Reference, ANSYS, Inc.
31. Newmark, N.M., *A Method of Computation for Structural Dynamics*. ASCE *Journal of Engineering Mechanics*, 1959. **85**(EM3).
32. Luo, C. P., *Detection of Antibody-Antigen Reactions Using Surface Acoustic Wave and Electrochemical Immunosensors*, in *Natural Sciences and Mathematics*. 2004, Ruperto-Carola University: Heidelberg. p. 131.
33. Yamanaka, K., Ishikawa, S., Nakaso, N., Takeda, N., Mihara, T. and Tsukahara, Y., *Ball SAW device for hydrogen gas sensor*. in *IEEE Ultrasonics Symposium*. 2003. Honolulu, HI, United States: Institute of Electrical and Electronics Engineers Inc., Piscataway, United States.
34. D'Amico, A. and Zemel, J. N., *Pyroelectric Enthalpimetric Detection*. *Journal of Applied Physics*, 1985. **57**(7): p. 2460-2463.
35. Butler, M.A., *Optical Fiber Hydrogen Sensor*. *Applied Physics Letters*, 1984. **45**(10): p. 1007-1009.
36. Kumar, R.V. and Fray, D. J., *Development OF Solid State Hydrogen Sensors*. *Sensors and Actuators*, 1988. **15**(2): p. 185-191.
37. Lukaszewski, M. and Czerwinski, A., *Electrochemical Quartz Crystal Microbalance Study on Hydrogen Absorption and Desorption into/from Palladium and Palladium-Noble Metal Alloys*. *Journal of Electroanalytical Chemistry*, 2006. **589**(1): p. 87-95.

38. Frazier, G.A. and Glosser, R., *Phase diagrams of thin films of the palladium hydrogen system using a quartz crystal thickness monitor*. Journal of Physics, D., 1979. **12**(10): p. L113-L115.
39. Christofides, C. and Mandelis, A., *Solid State Sensors for Trace Hydrogen Gas Detection*. Journal of Applied Physics, 1990. **68**(6): p. R1-R30.
40. Lewis, F.A., *The Palladium Hydrogen System*. 1967, London: Academic Press Inc.
41. Baranowski, B., Majchrzak, S. and Flanagan, T. B., *The Volume Increase of FCC Metals and Alloys due to Interstitial Hydrogen over a Wide Range of Hydrogen Contents*. Journal of Physics F: Metal Physics, 1971. **1**(3): p. 258-261.
42. Wicke, E., Brodowsky, H., *Hydrogen in Metals 2: Application Oriented Properties*. Topics in Applied Physics, ed. G. Alefeld, Vokl, J. Vol. 29. 1978, Berlin: Springer-Verlag.
43. Peisl, H., *Hydrogen in Metals 1: Basic Properties*. Topics in Applied Physics, ed. G. Alefeld, Vokl, J. Vol. 28. 1978, Berlin: Springer-Verlag.
44. Fabre, A., Finot, E., Demoment, J. and Contreras, S., *In situ measurement of elastic properties of PdHx, PdDx, and PdTx*. Journal of Alloys and Compounds, 2003. **356-357**: p. 372-376.
45. Madou, M.J., *Fundamentals of Microfabrication*. 2 ed. 2002: CRC Press.
46. Wong, K.K., ed. *Properties of Lithium Niobate*. 2002, INSPEC, The Institution for Electrical Engineers: London.
47. Didenko, I.S., Hickernell, F. S. and Naumenko, N., *The Experimental and Theoretical Characterization of the SAW Propagation Properties for Zinc Oxide Films on Silicon Carbide*. IEEE TRANSACTIONS ON ULTRASONICS, FERROELECTRICS, AND FREQUENCY CONTROL, 2000. **47**(1): p. 179-187.
48. ANSYS® Multiphysics, R., Help System, Coupled Field Analysis Guide, ANSYS, Inc.
49. Anisimkin, V.I., Kotelyanskii, I.M., Verardi, P. and Verona, E., *Elastic Properties of Thin-Film Palladium for Surface Acoustic Wave (SAW) Sensors*. Sensors and Actuators B, 1995. **23**(2-3): p. 203-208.
50. Rafizadeh, H., A., *Lattice Dynamics of Metal Hydrides*. Physical Review B, 1987. **23**(4): p. 1628-1632.

51. Atanackovic, T. M. and Guran, A., *Theory of Elasticity for Scientists and Engineers*. 2000, Boston: Springer.
52. Hietala, V.M., Casalnuovo, S.A., Heller, E.J., Wendt, J.R., Frye-Mason, G.C. and Baca, A.G., *Monolithic GaAs surface acoustic wave chemical microsensor array*. IEEE MTT-S International Microwave Symposium Digest, 2000. **3**: p. 1965-1968.
53. Hickernell, F.S., *Zinc Oxide Films for Acoustoelectric Device Applications*. IEEE Transactions on Sonics and Ultrasonics, 1985. **SU-32(5)**: p. 621-629.
54. Caliendo, C., Imperatori, P. and Cianci, E., *Structural Morphological and Acoustic Properties of AlN Thick Films Sputtered on Si(001) and Si(111) Substrates at Low Temperature*. Thin Solid Films, 2003. **441**: p. 32-37.
55. Caliendo, C., Verona, E. and Cimmino, A. *Microwave frequency acoustic resonators implemented on monolithic Si/AlN substrates*. in *Proceedings of the SPIE - The International Society for Optical Engineering*. 2001.
56. Tsubouchi, K. and Mikoshiba, N., *Zero Temperature Coefficient SAW Devices on AlN Epitaxial Films*. IEEE Transactions on Sonics and Ultrasonics, 1985. **SU-32(5)**: p. 634-644.
57. Ippolito, S.J., Kalantar-Zadeh, K., Powell, D. A. and Wlodarski, W. *A 3-Dimensional Approach for Simulating Acoustic Wave Propagation in Layered SAW Devices*. in *IEEE Ultrasonics Symposium*. 2003.

6.3 Appendix

A. Finite Element Codes

A.1 Finite Element Code for XY-LiNbO₃ ZnO Model

/FILNAME,
LAYEREDSUBFEWCPSETS17um, 0

/CONFIG,NPROC,2

/NERR, 100, 100, OFF

/PREP7

K, 1, 0, 0, 0

K, 2, 0, 500e-6, 0

K, 3, 1600e-6, 500e-6, 0

K, 4, 1600e-6, 0, 0

L, 1, 2

L, 2, 3

L, 3, 4

L, 4, 1

AL, 1, 2, 3, 4

CSYS, 11

! Changing the Element Coordinate
System for Subsequent Elements to be
Parallel to the Previously Defined
Local Coordinate System 11

! DEFINING MATERIAL TYPE

VOFFST, 1, 400e-6

K, 100, 0, 500e-6, 0

K, 101, 1600E-6, 500E-6, 0

K, 102, 1600E-6, 500E-6, -400E-6

K, 103, 0, 500E-6, -400E-6

L, 100, 101

L, 101, 102

L, 102, 103

L, 103, 100

AL, 13, 14, 15, 16

VOFFST, 7, 3e-6

VGLUE, 1, 2

CSKP, 11, 0, 1, 2, 4

CSKP, 20, 0, 1, 4, 5

ET, 1, SOLID226, 1001

! Defining The Material Properties Of
The Lithium Niobate Piezoelectric
Substrate

! Defining Material Properties OF
Lithium Niobate (Kg/m³)

```

MP, DENS, 1, 4647

! Defining The Dielectric
(Permittivity) Constants At Constant
Strain

TB, DPER,1,,0

TBDATA,1, 44.1 ,44.1, 23, 0, 0, 0

! Defining The Piezoelectric Stress
Matrix At Constant Strain

TB,PIEZ,1,,0

TBDATA,1, 0, -2.5, 0.2, 0, 2.5 ,0.2

TBDATA,7, 0, 0, 1.3, -2.5, 0, 0

TBDATA,13, 0, 3.7, 0, 3.7, 0, 0

! Defining The Elasticity Matrix In
Stiffness Form

TB,ANEL,1,,0

TBDATA,1, 2.03E11, 0.573E11,
0.752E11, 0, 0.085E11, 0

TBDATA,7, 2.03E11, 0.752E11, 0
,-0.085E11, 0, 2.424E11

TBDATA,13, 0, 0, 0, 0.728E11, 0,
0.085E11

TBDATA,19, 0.595E11, 0,
0.595E11

! Defining Material Properties of Zinc
Oxide

MP, DENS, 2, 5720

! Defining The Dielectric
(Permittivity) Constants At Constant
Strain

TBDATA,1, 8.3, 8.3, 8.8, 0, 0, 0

! Defining The Piezoelectric Stress
Matrix At Constant Strain

TB,PIEZ,2,,0

TBDATA,1, 0, 0, -0.51, 0, 0, -0.51

TBDATA,7, 0, 0, 1.22, 0,0 ,0

TBDATA,13, 0, -0.45, 0, -0.45, 0,
0

! Defining The Elasticity Matrix In
Stiffness Form

TB,ANEL,2,,0

TBDATA,1, 1.57e11, 0.89e11
,0.83e11, 0 , 0,0

TBDATA,7, 1.57e11,0.83e11, 0, 0,
0, 2.08e11

TBDATA,13, 0, 0, 0, 0.34e11, 0, 0

TBDATA,19, 0.38e11, 0, 0.38e11

!Meshing The Volume

VSEL, S, VOLU,,1, 1, 0

VATT, 1,,1,11

MSHAPE, 1

MSHKEY, 0

AESIZE, 4, 17e-6

MOPT, TETEXPND, 1.1

VMESH, 1, 1, 0

VSEL, ALL

VSEL, S, VOLU,,3, 3, 0

VATT, 2,,1, 20

```

```

ESIZE, 20e-6
VMESH, 3, 3, 0
NSEL, S, LOC, X, 500e-6
NSEL, R, LOC, Z, 90e-6, 310e-6
NSEL, R, LOC, Y, 600e-6, 1000e-6
NREFINE, ALL,,,1,5,CLEAN
VSEL, ALL

! Selecting And Grounding Input
Electrodes
ELEC = 3
*DIM, NTOP, ARRAY, ELEC
II=685e-6
JJ=695e-6
*DO, KK, 1, 2
NSEL, S, LOC, X, 500e-6
NSEL, R, LOC, Z, 100e-6, 300e-6
NSEL, R, LOC, Y, II, JJ
D, ALL, VOLT, 0
II=II+40e-6
JJ=JJ+40e-6
*ENDDO

!Coupling The Input Electrodes
II=705e-6
JJ=715e-6

*DO, KK, 1, 2
NSEL, S, LOC, X, 500e-6
NSEL, R, LOC, Z, 100e-6, 300e-6
NSEL, R, LOC, Y, II, JJ
CP, 1, VOLT, ALL
II=II+40e-6
JJ=JJ+40e-6
*ENDDO

NSEL, S, CP,,1
*GET, NTOP(1), CP, 1, TERM, 1,
NODE

! Selecting And Grounding Output
Electrodes
II=845e-6
JJ=855e-6
*DO, KK, 1, 2
NSEL, S, LOC, X, 500e-6
NSEL, R, LOC, Z, 100e-6, 300e-6
NSEL, R, LOC, Y, II, JJ
D, ALL, VOLT, 0
II=II+40e-6
JJ=JJ+40e-6
*ENDDO

!Coupling The Two Output Electrodes
Separately
NSEL, S, LOC, X, 500e-6
NSEL, R, LOC, Z, 100e-6, 300e-6

```



```

NSEL, R, LOC, Y, 865E-6, 875E-6
CP, 2, VOLT, ALL
*GET, NTOP(2), CP, 2, TERM, 1,
NODE
NSEL, ALL
NSEL, S, LOC, X, 500e-6
NSEL, R, LOC, Z, 100e-6, 300e-6
NSEL, R, LOC, Y, 905E-6, 915E-6
CP, 3, VOLT, ALL
*GET, NTOP(3), CP, 3, TERM, 1,
NODE
NSEL, ALL
!Constraining The Lower Area Of The
Piezoelectric Substrate
NSEL, S, LOC, X, 0
D, ALL, ALL, 0
NSEL, ALL
FINISH
/SOLU
ANTYPE, TRANS
TRNOPT, FULL,,,,,NMK
NLGEOM ,OFF
TINTP,,0.25, 0.5, 0.5
EQSLV, JCG

```

```

OUTRES, NSOL, ALL
KBC, 1
TIME, 0.5E-11
DELTIM, 0.5E-11
D, NTOP(1), VOLT, 1E9
SOLVE
KBC, 1
TIME, 1.005E-9
DELTIM, 1E-9
D, NTOP(1), VOLT, 1E9
SOLVE
KBC, 1
TIME, 100.005E-9
DELTIM, 1E-9
D, NTOP(1), VOLT,,
SOLVE
FINISH
/POST26
NSOL, 2, NTOP(2), VOLT,, NSOLV
NSOL, 3, NTOP(3), VOLT,, NSOLV
ADD, 4, 2, 3, ,VOLT, ,
XVAR, 1
PRVAR, 4

```

6.4 A.2 Finite Element Code for YZ-LiNbO₃ Model for Hydrogen Detection

```

/TITLE, pt1 H2 fc130

/FILNAME, pt1 H2 fc130, 0

/CONFIG,NPROC,2

/NERR, 100, 100, OFF

/PREP7

!Specifying Variables

Variables That I Input

*SET, SL , 3500e-6, !SUBSTRATE
LENGTH

*SET, EP , 12 !NUMBER OF
ELECTRODE PAIRS FOR EACH
IDT

!CALCULATED VARIABLES

*SET, LAMBDA, 26.5e-6
!WAVELENGTH

*SET, SD, 15*(34.88e-6)

!SEPARATION DISTANCE

*SET, LIED , (SL/2) - (SD/2)

!LAST INPUT ELECTRODE
DIMENSION

*SET, EW , LAMBDA/4
!ELECTRODE WIDTH

*SET, IDTL , (4*EP-1)*EW,
!LENGTH OF EACH IDT

*SET, FIED , LIED - IDTL !FIRST
INPUT ELECTRODE DIMENSION

*SET, FOED , (SL/2) + (SD/2),
!FIRST OUTPUT ELECTRODE
DIMENSION

*SET, VR, 0.019

*SET, FT, ((2e-6)*(1+VR))

*SET, ELEC , EP+1

! CREATING THE LiNbO3
SUBSTRATE

K, 1, 0,0,0

K, 2, 0,500e-6,0

K, 3, SL,500e-6,0

K, 4, SL,0,0

L, 1, 2

L, 2, 3

L, 3, 4

L, 4, 1

AL, 1, 2, 3, 4

VOFFSET, 1, 400E-6

!CREATING THE Pd Layer

K, 100, LIED + 50.1E-6 , 500e-6, -
112.475E-6

K, 101, FOED - 50.1E-6, 500E-6,-
112.475E-6

K, 102, FOED - 50.1E-6, 500E-6,-
287.525E-6

```

```

K, 103, LIED + 50.1E-6, 500E-6,-
287.525E-6
L, 100, 101
L, 101, 102
L, 102, 103
L, 103, 100
AL, 13, 14, 15, 16
VOFFST, 7, FT
VGLUE, ALL
!DEFINING A L.C.S for Y-Z LiNbO3
PROPERTIES
CSKP, 11, 0, 1, 5, 2
CSYS, 0
!Defining The Material Properties Of
The Lithium Niobate Piezoelectric
Substrate
ET, 1, SOLID226, 1001
! Defining Material Properties of
Lithium Niobate (Kg/m3)
MP, DENS, 1, 4647
! Defining The Dielectric
(Permittivity) Constants At Constant
Strain
TB, DPER,1,,0
TBDATA,1, 44.1, 44.1, 23, 0, 0 ,0
! Defining The Piezoelectric Stress
Matrix At Constant Strain
TB,PIEZ,1,,0
TBDATA,1, 0, -2.5, 0.2, 0, 2.5, 0.2
TBDATA,7, 0, 0, 1.3, -2.5, 0, 0
TBDATA,13, 0, 3.7, 0, 3.7, 0, 0
! Defining The Elasticity Matrix In
Stiffness Form
TB,ANEL,1,,0
TBDATA,1, 2.03E11, 0.573E11,
0.752E11, 0, 0.085E11, 0
TBDATA,7, 2.03E11, 0.752E11, 0,
-0.085E11, 0, 2.424E11
TBDATA,13, 0, 0, 0, 0.728E11, 0,
0.085E11
TBDATA,19, 0.595E11, 0,
0.595E11
!Defining The Material Properties of
Pd
ET, 2, SOLID98, 2
MP, EX, 2, 124.5E9
MP, DENS, 2, 12008.6
MP, PRXY, 2, 0.375
!Meshing The LiNbO3
VSEL, S, VOLU,,3, 3, 0
VATT, 1,,1,11
MSHAPE, 1
MSHKEY, 0
AESIZE, 13, 14e-6
MOPT, TETEXPND, 1.1
VMESH, 3, 3, 0
NSEL, S, LOC, Y, 500e-6

```

NSEL, R, LOC, Z, -300e-6, -100e-6

NSEL, R, LOC, X, FIED, FOED +
IDTL

NREFINE, ALL,,,1,2,CLEAN

VSEL, ALL

!Meshing The Pd Film

VSEL, S, VOLU,,2, 2, 0

VATT, 2,,2

ESIZE, 2e-6

VMESH, 2, 2, 0

VSEL, ALL

*DIM, NTOP, ARRAY, ELEC

!Selecting And Grounding Electrodes
Of Input Idt

II = FIED

JJ = II + EW

*DO, KK, 1, EP

ASEL, S, AREA,, 13, 13, 0

NSLA, S, 1

NSEL, R, LOC, Z, -300E-6, -100E-6

NSEL, R, LOC, X, II, JJ

D, ALL, VOLT, 0

II=II + LAMBDA

JJ=JJ + LAMBDA

*ENDDO

!Coupling The Input Electrodes

III = FIED + 2*EW

JJJ=III + EW

*DO, KK, 1, EP

ASEL, S, AREA,, 13, 13, 0

NSLA, S, 1

NSEL, R, LOC, Z, -300E-6, -100E-6

NSEL, R, LOC, X, III, JJJ

CP, 1, VOLT, ALL

III=III + LAMBDA

JJJ=JJJ + LAMBDA

*ENDDO

NSEL, S, CP,,1

*GET, NTOP(1), CP, 1, TERM, 1,
NODE

!Selecting And Grounding Electrodes
Of Output Idt

II = FOED

JJ = II + EW

*DO, KK, 1, EP

ASEL, S, AREA,, 13, 13, 0

NSLA, S, 1

NSEL, R, LOC, Z, -300E-6, -100E-6

NSEL, R, LOC, X, II, JJ

D, ALL, VOLT, 0

II=II + LAMBDA

JJ=JJ + LAMBDA

```

*ENDDO

!Coupling The Output Electrodes
Separately

III = FOED + 2*EW

JJJ = III + EW

*DO, KK, 2, ELEC

ASEL, S, AREA,, 13, 13, 0

NSLA, S, 1

NSEL, R, LOC, Z, -300E-6, -100E-6

NSEL, R, LOC, X, III, JJJ

CP, KK, VOLT, ALL

*GET, NTOP(KK), CP, KK, TERM,
1, NODE

III = III + LAMBDA

JJJ = JJJ + LAMBDA

NSEL, ALL

*ENDDO

!GROUNDING ELECTRODES ON
PROPAGATION PATH

ASEL, S, AREA,, 13, 13, 0

NSLA, S, 1

NSEL, R, LOC, Z, -287.525E-6, -
112.475E-6

NSEL, R, LOC, X, LIED+50.1E-6,
FOED-50.1E-6

CP, ELEC+1, VOLT, ALL

!Constraining The Lower Area Of The
Piezoelectric Substrate

NSEL, S, LOC, Y, 0

D, ALL, ALL, 0

NSEL, ALL

FINISH

/SOLU

TME = 400E-9

ANTYPE, TRANS

TRNOPT, FULL,,,,,NMK

NLGEOM ,OFF

TINTP,,0.25, 0.5, 0.5

EQSLV, SPARSE

OUTRES, NSOL, ALL

KBC, 1

TIME, 0.5E-11

DELTIM, 0.5E-11

D, NTOP(1), VOLT, 1E9

SOLVE

KBC, 1

TIME, 1.005E-9

DELTIM, 1E-9

D, NTOP(1), VOLT, 1E9

SOLVE

KBC, 1

TIME, TME

DELTIM, 1E-9

```

SOLVE	*VOPER, TT(1,1), RR(1,1), ADD, RR(1,2)
FINISH	
/POST26	*DO, KK, 1, EP-2
NUMVAR, 30	*VOPER, TT(1, KK+1), TT(1, KK), ADD, RR(1, KK+2)
*DO, KK, 2, EP+1	*ENDDO
NSOL, KK, NTOP(KK), VOLT	*CREATE, WRITEIT3, MAC
STORE, MERGE	*CFOPEN, pt1H2fc130, TXT
*ENDDO	*VWRITE, TT(1, EP-1)
*GET, SIZE, VARI, NSETS	%16.9G
*DIM, RR, ARRAY, SIZE, EP	*CFCLOSE
*DO, KK, 2, EP+1	*END
VGET, RR(1, KK-1), KK	WRITEIT3
*ENDDO	
*DIM, TT, ARRAY, SIZE, EP-1	

6.5

6.6 A.3 Finite Element Code for AlN/Si(111) Reduced 3D Model

/TITLE, Q2D EP10 H6 L30

/FILENAME, Q2D EP10 H6 L30, 0

/CONFIG,NPROC,4

/NERR, 100, 100, OFF

/PREP7

!SPECIFYING VARIABLES

!VARIABLES THAT I INPUT

*SET, SL , 2000e-6 !SUBSTRATE LENGTH

*SET, EP , 10 !NUMBER OF ELECTRODE PAIRS FOR EACH IDT

*SET, H , 6e-6 !THICKNESS OF THE ALUMINUM NITRIDE FILM

*SET, TH, 11E-6 !THICKNESS OF THE REDUCED MODEL

!CALCULATED VARIABLES

*SET, LAMBDA, 30e-6
!WAVELENGTH

*SET, SD 2*LAMBDA
!SEPARATION DISTANCE

*SET, LIED , (SL/2) - (SD/2)

!LAST INPUT ELECTRODE DIMENSION

*SET, EW , LAMBDA/4
!ELECTRODE WIDTH

*SET, IDTL , (4*EP-1)*EW
!LENGTH OF EACH IDT

*SET, FIED , LIED - IDTL

!FIRST INPUT ELECTRODE DIMENSION

*SET, FOED , (SL/2) + (SD/2)

!FIRST OUTPUT ELECTRODE DIMENSION

*SET, ELEC , EP+1

! CREATING THE SILICON SUBSTRATE

K, 1, 0,0, 0

K, 2, 0,500e-6, 0

K, 3, SL, 500e-6, 0

K, 4, SL, 0, 0

L, 1, 2

L, 2, 3

L, 3, 4

L, 4, 1

AL, 1, 2, 3, 4

VOFFSET, 1, TH

CSYS, 0

!SPECIFYING THE C.S FOR THE [111] ORIENTATION

K, 201, 78.87E-6, 57.74E-6, -21.13E-6	! Defining Material Properties For Silicon
K, 202, -57.74E-6, 57.74E-6, -57.74E-6	! Defining The Elasticity Matrix In Stiffness Form (N/m ²)
CSKP, 20, 0, 1, 201, 202	TB,ANEL,1,,0
CSYS, 0	TBDATA,1, 1.66E11, 0.64E11, 0.64E11, 0, 0, 0
! Creating Aluminum Nitride Thin Film	TBDATA,7, 1.66E11, 0.64E11, 0, 0, 0, 1.66E11
K, 101, 0, 500E-6, 0	TBDATA,13, 0, 0, 0, 0.8E11, 0, 0
K, 102, 0, 500E-6 + H, 0	TBDATA,19, 0.8E11, 0, 0.8E11
K, 103, SL, 500E-6 + H, 0	MP, DENS, 1, 2320
K, 104, SL, 500E-6, 0	! Defining Element Type For The AlN Film
L, 101, 102	ET, 2, SOLID226, 1001
L, 102, 103	! Defining Material Properties for Aluminum Nitride
L, 103, 104	MP, DENS, 2, 3260
L, 104, 101	! Defining The Dielectric (Permittivity) Constants At Constant Strain
AL, 13, 14, 15, 16	TB, DPER,2,,0
VOFFSET, 7, TH	TBDATA,1, 9.04, 9.04, 10.73, 0, 0, 0
ASEL, ALL	! Defining The Piezoelectric Stress Matrix At Constant Strain (C/m ²)
VGLUE, ALL	TB,PIEZ,2,,0
! Specifying The Orientation For C-Axis Aln Film	TBDATA,1, 0, 0, -0.58, 0, 0, -0.58
CSKP, 30, 0, 1, 4, 5	TBDATA,7, 0, 0, 1.55, 0, 0, 0
CSYS, 0	TBDATA,13, 0, -0.48, 0, -0.48, 0, 0
! Defining Element Type For The Silicon	
ET, 1, SOLID98, 2	

! Defining The Elasticity Matrix In
Stiffness Form (N/m²)

TB,ANEL,2,,0

TBDATA,1, 3.45E11, 1.25E11,
1.2E11, 0, 0, 0

TBDATA,7, 3.45E11, 1.2E11, 0, 0,
0, 3.95E11

TBDATA,13, 0, 0, 0, 1.1E11, 0, 0

TBDATA,19, 1.18E11, 0, 1.18E11

!Meshing The Silicon

VSEL, S, VOLU,,1, 1, 0

VATT, 1,,1,20

MSHAPE, 1

MSHKEY, 0

AESIZE, 4, 3e-6

MOPT, TETEXPND, 1.1

VMESH, 1, 1, 0

VSEL, ALL

!Meshing The AlN Film

VSEL, S, VOLU,,3, 3, 0

VATT, 2,,2,30

ESIZE, 3e-6

VMESH, 3, 3, 0

VSEL, ALL

*DIM, NTOP, ARRAY, ELEC

!Selecting And Grounding Electrodes
Of Input Idt

II = FIED

JJ = II + EW

*DO, KK, 1, EP

ASEL, S, AREA,, 10, 10, 0

NSLA, S, 1

NSEL, R, LOC, X, II, JJ

D, ALL, VOLT, 0

II=II + LAMBDA

JJ=JJ + LAMBDA

*ENDDO

!Coupling The Input Electrodes

III = FIED + 2*EW

JJJ=III + EW

*DO, KK, 1, EP

ASEL, S, AREA,, 10, 10, 0

NSLA, S, 1

NSEL, R, LOC, X, III, JJJ

CP, 1, VOLT, ALL

III=III + LAMBDA

JJJ=JJJ + LAMBDA

*ENDDO

NSEL, S, CP,,1

*GET, NTOP(1), CP, 1, TERM, 1,
NODE

!Selecting And Grounding Electrodes
Of Output IDT

```

II = FOED
JJ = II + EW
*DO, KK, 1, EP
ASEL, S, AREA,, 10, 10, 0
NSLA, S, 1
NSEL, R, LOC, X, II, JJ
D, ALL, VOLT, 0
II=II + LAMBDA
JJ=JJ + LAMBDA
*ENDDO

!Coupling The Output Electrodes
Separately

III = FOED + 2*EW
JJJ = III + EW
*DO, KK, 2, ELEC
ASEL, S, AREA,, 10, 10, 0
NSLA, S, 1
NSEL, R, LOC, X, III, JJJ
CP, KK, VOLT, ALL
*GET, NTOP(KK), CP, KK, TERM,
1, NODE
III = III + LAMBDA
JJJ = JJJ + LAMBDA
NSEL, ALL
*ENDDO

```

```

!Constraining The Lower Area Of The
Piezoelectric Substrate

```

```

NSEL, S, LOC, Y, 0
D, ALL, ALL, 0
NSEL, ALL
FINISH
/SOLU
TME = 200E-9
ANTYPE, TRANS
TRNOPT, FULL,,,,,NMK
NLGEOM ,OFF
TINTP,,0.25, 0.5, 0.5
EQSLV, SPARSE
OUTRES, NSOL, ALL
KBC, 1
TIME, 0.5E-11
DELTIM, 0.5E-11
D, NTOP(1), VOLT, 1E9
SOLVE
KBC, 1
TIME, 1.005E-9
DELTIM, 1E-9
D, NTOP(1), VOLT, 1E9
SOLVE
KBC, 1
TIME, TME

```

```
DELTIM, 1E-9
SOLVE
FINISH
/POST26
NUMVAR, 50
*DO, KK, 2, EP+1
NSOL, KK, NTOP(KK), VOLT
STORE, MERGE
*ENDDO
*GET, SIZE, VARI,,NSETS
*DIM, RR, ARRAY, SIZE, EP
*DO, KK, 2, EP+1
VGET, RR(1, KK-1), KK
*ENDDO
*DIM, TT, ARRAY, SIZE, EP-1
*VOPER, TT(1,1), RR(1,1), ADD,
RR(1,2)
*DO, KK, 1, EP-2
*VOPER, TT(1, KK+1), TT(1, KK),
ADD, RR(1, KK+2)
*ENDDO
*CREATE, WRITEIT2, MAC
*CFOPEN, IRQ2DEP5H6L30, TXT
*VWRITE, TT(1, EP-1)
%16.9G
*CFCLOSE
```

```
*END
```

```
WRITEIT2
```

A.4 Finite Element Code for AlN/Si(111) 2D Model

/CLEAR, START

/TITLE, 2D Model H6L30

/FILENAME, 2D Model H6L30, 0

/CONFIG,NPROC,4

/NERR, 100, 100, OFF

/PREP7

!SPECIFYING VARIABLES

!VARIABLES THAT I INPUT

*SET, SL, 2000e-6 !SUBSTRATE
LENGTH

*SET, EP, 10 !NUMBER OF
ELECTRODE PAIRS FOR EACH
IDT

*SET, H, 6e-6 !THICKNESS OF THE
ALUMINUM NITRIDE FILM

!CALCULATED VARIABLES

*SET, LAMBDA, 30e-6
!WAVELENGTH

*SET, SD, 2*LAMBDA
!SEPARATION DISTANCE

*SET, LIED, (SL/2) - (SD/2)

!LAST INPUT ELECTRODE
DIMENSION

*SET, EW, LAMBDA/4
!ELECTRODE WIDTH

*SET, IDTL, (4*EP-1)*EW
!LENGTH OF EACH IDT

*SET, FIED, LIED - IDTL

!FIRST INPUT ELECTRODE
DIMENSION

*SET, FOED, (SL/2) + (SD/2)

!FIRST OUTPUT ELECTRODE
DIMENSION

*SET, ELEC, EP+1

! CREATING THE SILICON
SUBSTRATE

K, 1, 0,0, 0

K, 2, 0,500e-6, 0

K, 3, SL, 500e-6, 0

K, 4, SL, 0, 0

L, 1, 2

L, 2, 3

L, 3, 4

L, 4, 1

AL, 1, 2, 3, 4

CSYS, 0

! CREATING ALUMINUM NITRIDE
THIN FILM

K, 101, 0, 500E-6, 0

K, 102, SL, 500E-6, 0

K, 103, SL, 500E-6 + H, 0

K, 104, 0, 500E-6 + H, 0

L, 101, 102

L, 102, 103

```

L, 103, 104
L, 104, 101
AL, 5, 6, 7, 8
ASEL, ALL
AGLUE, ALL

! Defining Element Type For The Silicon
ET, 1, PLANE13, 3

! Defining Material Properties For Silicon
! Defining The Elasticity Matrix In Stiffness Form (N/m^2)
TB,ANEL,1,,0
TBDATA,1, 1.95E11, 0.4467E11, 0.5433E11, 0.0811E11
TBDATA,7, 2.0467E11 , 0.4467E11, -0.3556E11
TBDATA,12, 1.95E11
TBDATA,13, 0.2744E11
TBDATA,16, 0.6067E11
MP, DENS, 1, 2320

! DEFINING ELEMENT TYPE FOR THE AIN FILM
ET, 2, PLANE223, 1001

! Defining Material Properties for Aluminum Nitride
MP, DENS, 2, 3260

! Defining The Dielectric (Permittivity) Constants At Constant Strain
TB, DPER,2,,0
TBDATA,1, 9.04, 10.73
TBDATA,4, 0

! Defining The Piezoelectric Stress Matrix At Constant Strain (C/m^2)
TB,PIEZ,2,,0
TBDATA,1, 0, 0.58,0 , 0, -1.55, 0
TBDATA,7, 0, 0.58,0,0.48,0,0

! Defining The Elasticity Matrix In Stiffness Form (N/m^2)
TB,ANEL,2,,0
TBDATA,1, 3.45E11, 1.2E11, 1.25E11, 0
TBDATA,7, 3.95E11, 1.2E11 ,0
TBDATA,12, 3.45E11
TBDATA,13, 0
TBDATA,16, 1.18E11

!Meshing The Silicon
ASEL, S, AREA,,1, 1, 0
AATT, 1,,1,0
MSHAPE, 1
LESIZE, 2, 2e-6,,,,,100e-6,-2
AMESH, 1, 1, 0
ASEL, ALL

```

```

!MESHING THE Aln FILM
ASEL, S, AREA,,3, 3, 0
AATT, 2,,2,0
ESIZE, 2e-6
AMESH, 3, 3, 0
ASEL, ALL
*DIM, NTOP, ARRAY, ELEC
!Selecting And Grounding Electrodes
Of Input IDT
II = FIED
JJ = II + EW
*DO, KK, 1, EP
LSEL, S, LINE, ,7, 7, 0
NSLL, S, 1
NSEL, R, LOC, X, II, JJ
D, ALL, VOLT, 0
II=II + LAMBDA
JJ=JJ + LAMBDA
*ENDDO
!Coupling The Input Electrodes
III = FIED + 2*EW
JJJ=III + EW
*DO, KK, 1, EP
LSEL, S, LINE, ,7, 7, 0
NSLL, S, 1
NSEL, R, LOC, X, III, JJJ
CP, 1, VOLT, ALL
III=III + LAMBDA
JJJ=JJJ + LAMBDA
*ENDDO
NSEL, S, CP,,1
*GET, NTOP(1), CP, 1, TERM, 1,
NODE
!Selecting And Grounding Electrodes
Of Output IDT
II = FOED
JJ = II + EW
*DO, KK, 1, EP
LSEL, S, LINE, ,7, 7, 0
NSLL, S, 1
NSEL, R, LOC, X, II, JJ
D, ALL, VOLT, 0
II=II + LAMBDA
JJ=JJ + LAMBDA
*ENDDO
!Coupling The Output Electrodes
Separately
III = FOED + 2*EW
JJJ = III + EW
*DO, KK, 1, EP
LSEL, S, LINE, ,7, 7, 0
NSLL, S, 1

```

NSEL, R, LOC, X, III, JJJ	SOLVE
CP, KK+1, VOLT, ALL	KBC, 1
*GET, NTOP(KK+1), CP, KK+1, TERM, 1, NODE	TIME, 1.005E-9
III = III + LAMBDA	DELTIM, 1E-9
JJJ = JJJ + LAMBDA	D, NTOP(1), VOLT, 1E9
NSEL, ALL	SOLVE
*ENDDO	KBC, 1
!Constraining The Lower Area Of The Piezoelectric Substrate	TIME, TME
NSEL, S, LOC, Y, 0	DELTIM, 1E-9
D, ALL, ALL, 0	SOLVE
NSEL, ALL	FINISH
FINISH	/POST26
/SOLU	NUMVAR, 50
TME = 200E-9	*DO, KK, 2, EP+1
ANTYPE, TRANS	NSOL, KK, NTOP(KK), VOLT
TRNOPT, FULL,,,,,NMK	STORE, MERGE
NLGEOM, OFF	*ENDDO
TINTP,,0.25, 0.5, 0.5	*GET, SIZE, VARI,,NSETS
EQSLV, SPARSE	*DIM, RR, ARRAY, SIZE, EP
OUTRES, NSOL, ALL	*DO, KK, 2, EP+1
KBC, 1	VGET, RR(1, KK-1), KK
TIME, 0.5E-11	*ENDDO
DELTIM, 0.5E-11	*DIM, TT, ARRAY, SIZE, EP-1
D, NTOP(1), VOLT, 1E9	*VOPER, TT(1,1), RR(1,1), ADD, RR(1,2)
	*DO, KK, 1, EP-2

*VOPER, TT(1, KK+1), TT(1, KK),
ADD, RR(1, KK+2)

*ENDDO

*CREATE, WRITEIT2, MAC

*CFOPEN, 2DH6L30, TXT

*VWRITE, TT(1, EP-1)

%16.9G

*CFCLOSE

*END

WRITEIT2